

IRAK4 Dimerization and *trans*-Autophosphorylation Are Induced by Myddosome Assembly

Ryan Ferrao,^{1,2,3} Hao Zhou,⁴ Yibing Shan,⁵ Qun Liu,⁶ Qiubai Li,^{1,2} David E. Shaw,^{5,7} Xiaoxia Li,⁴ and Hao Wu^{1,2,3,*}

¹Department of Biological Chemistry and Molecular Pharmacology, Harvard Medical School, Boston, MA 02115, USA

²Program in Cellular and Molecular Medicine, Boston Children's Hospital, Boston, MA 02115, USA

³Weill Cornell Graduate School of Medical Sciences, New York, NY 10065, USA

⁴Department of Immunology, Lerner Research Institute, Cleveland Clinic Foundation, Cleveland, OH 44195, USA

⁵D.E. Shaw Research, New York, NY 10036, USA

⁶New York Structural Biology Center, National Synchrotron Light Source X4, Brookhaven National Laboratory, Upton, NY 11961, USA

⁷Department of Biochemistry and Molecular Biophysics, Columbia University, New York, NY 10032, USA

*Correspondence: hao.wu@childrens.harvard.edu

<http://dx.doi.org/10.1016/j.molcel.2014.08.006>

SUMMARY

trans-autophosphorylation is among the most prevalent means of protein kinase activation, yet its molecular basis is poorly defined. In Toll-like receptor and interleukin-1 receptor signaling pathways, the kinase IRAK4 is recruited to the membrane-proximal adaptor MyD88 through death domain (DD) interactions, forming the oligomeric Myddosome and mediating NF- κ B activation. Here we show that unphosphorylated IRAK4 dimerizes in solution with a K_D of 2.5 μ M and that Myddosome assembly greatly enhances IRAK4 kinase domain (KD) autophosphorylation at sub- K_D concentrations. The crystal structure of the unphosphorylated IRAK4^{KD} dimer captures a conformation that appears to represent the actual *trans*-autophosphorylation reaction, with the activation loop phosphosite of one IRAK4 monomer precisely positioned for phosphotransfer by its partner. We show that dimerization is crucial for IRAK4 autophosphorylation in vitro and ligand-dependent signaling in cells. These studies identify a mechanism for oligomerization-driven allosteric autoactivation of IRAK4 that may be general to other kinases activated by autophosphorylation.

INTRODUCTION

Toll-like receptors (TLRs) and interleukin-1 (IL-1) receptors (IL-1Rs) form a large family of transmembrane receptors that function in inflammatory and innate immune signaling (Kawai and Akira, 2010; Netea et al., 2012). TLR family members are expressed in a variety of immune cells, each recognizing a distinct pathogen-associated molecular pattern, such as dsRNA, lipopolysaccharides, flagellin, and unmethylated CpG DNA, using extracellular leucine-rich repeat (LRR) domains. IL-1R family members recognize cognate agonistic cytokines such as IL-1 β and IL-18 using extracellular immunoglobulin-like domains.

Structural information on TLR-ligand complexes reveals that LRR domains form similar M-shaped dimers that bring their C termini in close proximity to each other for signal initiation (Jin and Lee, 2008). Crystal structures of a ternary complex comprised of IL-1R, the coreceptor IL-1RAcP, and IL-1 β also demonstrate adjacent receptor and coreceptor C termini (Thomas et al., 2012; Wang et al., 2010).

Members of the TLR and IL-1R families share a common cytoplasmic Toll/IL-1 receptor (TIR) domain that is essential for the initiation of intracellular signaling (Ferrao et al., 2012; Netea et al., 2012). Ligand binding promotes receptor oligomerization, resulting in juxtaposition of receptor TIR domains and recruitment of TIR-containing adaptor proteins. MyD88 is the most critical of these adaptors, being essential for IL-1R signaling and all TLR family members except TLR3. MyD88 recruits IL-1R-associated kinase (IRAK) family members, directly interacting with IRAK4, the most proximal IRAK, followed by the downstream kinases IRAK1 and IRAK2. Activation of IRAKs results in formation of the TRAF6-TAK1-IKK signalosome for induction of the NF- κ B pathway through polyubiquitination and kinase activation (Ferrao et al., 2012). The importance of MyD88 and IRAK4 in human diseases is exemplified by the prevalence of gain-of-function MyD88 mutations in diffuse large B cell lymphoma and Waldenström's macroglobulinemia (Ngo et al., 2011; Treon et al., 2012), as well as loss-of-function MyD88 and IRAK4 mutations in children with recurrent pyogenic bacterial infections (Picard et al., 2003; von Bernuth et al., 2008).

MyD88 and IRAKs all contain a death domain (DD) (Figure 1A), a small α -helical domain that is highly prevalent in immune signaling complexes. Recruitment of IRAKs to MyD88 at the membrane is mediated by formation of an oligomeric DD scaffold, the Myddosome (Motshwene et al., 2009). Our previous crystal structure of this scaffold revealed six MyD88 DDs, four IRAK4 DDs, and four IRAK2 DDs in a helically symmetrical sequential arrangement, providing insight into the elegant ordered assembly mechanism (Lin et al., 2010). Consistent with previous results, IRAK4 is the most upstream kinase in the pathway and is capable of autophosphorylation (Cheng et al., 2007; Li et al., 2002). In addition, activated IRAK4 phosphorylates the activation loop of the downstream kinases IRAK1 and IRAK2, and MyD88 has been shown to promote this phosphorylation (Li et al., 2002).

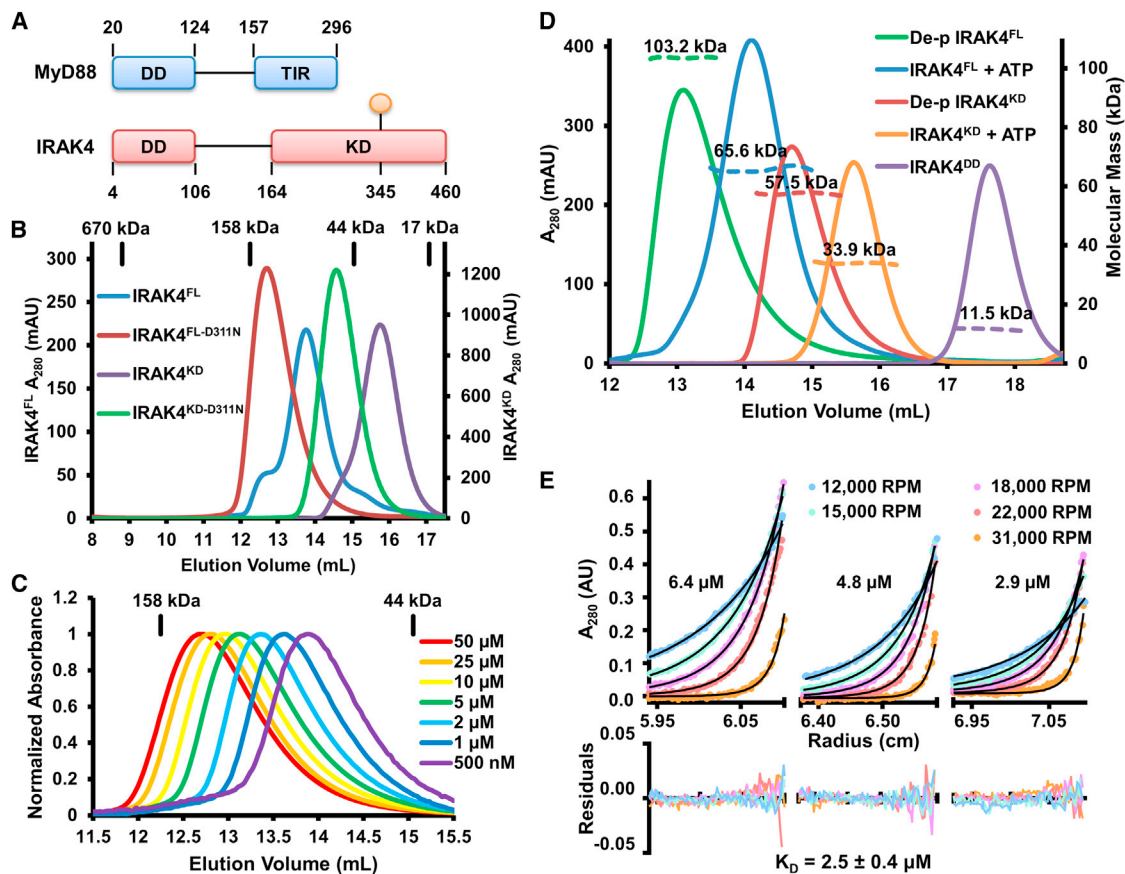


Figure 1. Unphosphorylated IRAK4 Is Dimeric

(A) Domain organization of IRAK4 and MyD88. Approximate domain boundaries are labeled with residue numbers, and the prototypical phosphorylation site at T345 is shown in orange.

(B) Size-exclusion chromatograms of full-length and kinase domain of IRAK4 (IRAK4^{FL} and IRAK4^{KD}) and their catalytically inactive forms (IRAK4^{FL-D311N} and IRAK4^{KD-D311N}). Elution volumes of protein standards are indicated above.

(C) Normalized size-exclusion chromatograms of IRAK4^{FL-D311N} at different concentrations.

(D) Size-exclusion chromatograms (solid lines) and molecular mass as measured by multiangle light scattering (MALS) (dotted lines) of dephosphorylated (de-p) IRAK4^{FL} and IRAK4^{KD}, IRAK4^{FL} and IRAK4^{KD} after ATP/Mg²⁺ incubation, and the IRAK4 death domain (IRAK4^{DD}).

(E) Sedimentation equilibrium analytical ultracentrifugation of IRAK4^{FL-D311N} at 6.4 μ M, 4.8 μ M, and 2.9 μ M. Samples were run at five different speeds shown in rpm. Solid black lines correspond to the fitting of a monomer-dimer self-association model, which produced a dimerization K_D of 2.5 ± 0.4 μ M. Residuals are plotted below.

See also Figure S1.

Many immune signaling complexes are now known to be higher-order assemblies that function as platforms for the activation of enzymes such as kinases and caspases (Wu, 2013). Oligomerization-driven kinase activation may be mediated by autophosphorylation between two identical kinase molecules, likely in *trans*, although activation in *cis* has been implicated in other systems (Hu et al., 2013; Pellicena and Kuriyan, 2006). In the case of IRAK4, a previous report implicated a *cis*-autophosphorylation mechanism, as wild-type (WT) IRAK4 was unable to phosphorylate a kinase-dead IRAK4 in their experiments (Cheng et al., 2007).

Here, we used a combination of biochemistry, structural biology, and cell biology to reveal the molecular mechanism of IRAK4 autoactivation in the Myddosome. We showed that, surprisingly, unphosphorylated but not phosphorylated IRAK4

kinase domain (KD) is dimeric in solution with a modest dimerization constant. Previous structural studies on kinase autophosphorylation have been hampered by the transient nature of the process and relied on analysis of crystal lattice interactions. The crystal structure of the IRAK4 dimer revealed in this study instead allowed visualization of the native interactions in solution and permitted direct assessment of the role of IRAK4 dimerization in autophosphorylation and signaling. We demonstrated that IRAK4 undergoes *trans*-autophosphorylation rather than *cis*-autophosphorylation and that the asymmetric unphosphorylated IRAK4^{KD} dimer structure caught in an enzyme-substrate embrace represents a bona fide *trans*-autophosphorylation conformation that is promoted by the Myddosome. Our studies uncovered the proximity-enhanced allosteric changes required for IRAK4 activation,

which may represent a common mechanism of kinase *trans*-autophosphorylation.

RESULTS

Unphosphorylated, but Not Phosphorylated, IRAK4 Forms Dimers in Solution

In order to capture the conformation of IRAK4 in the Myddosome during the initial autophosphorylation event, we reasoned that IRAK4 should be unphosphorylated. We therefore mutated the conserved Asp311 in the catalytic loop of full-length IRAK4 (IRAK4^{FL}) to an Asn (IRAK4^{FL-D311N}). This residue interacts with the attacking hydroxyl side chain of the substrate and is required for phosphotransfer (Nolen et al., 2004). We expressed His-tagged IRAK4^{FL-D311N} and coexpressed a His-IRAK4^{FL-D311N}/MyD88^{DD} complex in insect cells (Figure S1A, available online) with the goal of crystallization. Surprisingly, the size-exclusion chromatography (SEC) elution position of IRAK4^{FL-D311N} suggested that it was dimeric in solution (Figure 1B). When analyzed at different concentrations with SEC, IRAK4^{FL-D311N} eluted as single peaks rather than two distinct monomer and dimer peaks (Figure 1C). These peaks shifted from a dimeric position toward a monomeric one as the concentration was lowered, suggestive of a dynamic monomer/dimer equilibrium.

We initially speculated that this dimerization was mediated by the DD of IRAK4, as many DDs are capable of homooligomerization (Ferrao and Wu, 2012). To test this hypothesis, we expressed and purified the IRAK4 KD containing the D311N mutant (IRAK4^{KD-D311N}). Unexpectedly, IRAK4^{KD-D311N} also appeared dimeric by SEC analysis (Figure 1B), suggesting that IRAK4 dimerization is mediated by the KD. In agreement, a construct containing only the DD of IRAK4 has an experimental molecular mass of 11.5 kDa (3.0% error) as measured by multiangle light scattering (MALS), consistent with the 11.9 kDa calculated monomeric molecular mass (Figure 1D).

Because previously crystallized phosphorylated IRAK4 KD (p-IRAK4^{KD}) was monomeric in solution (Kuglstatter et al., 2007), we suspected that IRAK4 dimerization is affected by the phosphorylation state of the kinase. Therefore, we expressed and purified WT IRAK4^{FL} and IRAK4^{KD} from insect cells. IRAK4^{FL} was judged to be active by phosphorylation of an IRAK1 activation loop peptide (Figure S1B). The IRAK4 activation loop contains three phosphorylation sites, T342, T345, and S346 (Cheng et al., 2007), with T345 as the prototypical phosphoresidue responsible for phosphorylation-dependent activation loop stabilization and kinase activation (Kuglstatter et al., 2007). Western blot analysis with an antibody generated to react with an IRAK4 pT345-containing phosphopeptide showed that IRAK4^{FL} was natively phosphorylated and that this phosphorylation could be removed by treatment with λ -phosphatase (Figure S1C). Upon incubation of IRAK4^{FL} with ATP/Mg²⁺, T345 phosphorylation increased (Figure S1D). In comparison, IRAK4^{FL-D311N} had inappreciable levels of native T345 phosphorylation, and no additional phosphorylation was detected upon ATP/Mg²⁺ incubation (Figure S1D). Liquid chromatography-tandem mass spectrometry (LC-MS/MS) revealed that IRAK4^{FL} is phosphorylated at T345, T342, and S346, with the most significant phosphorylation occurring at the pro-

typical T345 residue (Figure S1E). Importantly, both natively phosphorylated IRAK4^{FL} and IRAK4^{KD} appeared primarily monomeric when subjected to SEC analysis (Figure 1B).

To further determine if IRAK4 phosphorylation states play a role in the monomer-to-dimer transition, we first dephosphorylated IRAK4^{FL} with λ -phosphatase. Dephosphorylated IRAK4^{FL} was analyzed by mass spectrometry, and no residual phosphorylation was detected on any of the activation loop residues (Figure S1E). Dephosphorylated IRAK4^{FL} is dimeric in solution, with an experimental molecular mass of 103.2 kDa (0.8% error) as measured by MALS (Figure 1D), approximating the calculated dimer molecular mass of 103.8 kDa. Incubation with ATP/Mg²⁺ results in autophosphorylation of IRAK4^{FL} and a shift toward a monomeric molecular mass, 65.6 kDa (1.0% error) by MALS (Figure 1D). Similarly, dephosphorylated IRAK4^{KD} is also dimeric with a measured molecular mass of 57.5 kDa (0.5% error) (Figure 1D), in comparison with the calculated monomer molecular weight of 34.8 kDa. Following treatment with ATP/Mg²⁺, autophosphorylated IRAK4^{KD} becomes monomeric, with an experimental molecular mass of 33.9 kDa (0.8% error) (Figure 1D).

In order to investigate the thermodynamic parameters of IRAK4 dimerization, we performed sedimentation equilibrium analytical ultracentrifugation (SE-AUC) on IRAK4^{FL-D311N} at concentrations of 6.4 μ M, 4.8 μ M, and 2.9 μ M (Figure 1E). Centrifugation at five speeds followed by global fitting of a monomer-dimer self-association model resulted in a measured dimerization constant (K_D) of $2.5 \pm 0.4 \mu$ M, a modest affinity in protein-protein interactions.

IRAK4 *trans*-Autophosphorylation Is Enhanced by MyD88

The dimerization constant and the equilibrium behavior of IRAK4 during SEC suggest a dynamic dimerization that may not occur in cells in the resting state. Because IRAK4 gets recruited to the Myddosome through DD/DD interactions with MyD88, we next sought to understand the effect of MyD88 on IRAK4 autophosphorylation and therefore signaling-dependent IRAK4 activation. An *in vitro* assay of IRAK4 autophosphorylation would require soluble recombinant MyD88. Although MyD88^{DD} can form a well-defined complex when coexpressed with IRAK4^{FL-D311N} (Figure S1A), MyD88^{DD} alone has the propensity to form insoluble aggregates. Even the best-behaved construct of MyD88 (20–154), containing the DD and additional linker residues, still exhibits poor solubility and forms high molecular weight aggregates when analyzed by SEC (Figure 2A).

In the crystal structure of the ternary Myddosome DD complex (Lin et al., 2010), a layer of MyD88 interacts with a layer of IRAK4 using one surface while simultaneously utilizing a distinct interface to mediate MyD88 homotypic interactions (Figure 2B). Therefore, we postulated that the ability of MyD88 to aggregate was dependent on the interaction between these two MyD88 layers. To disrupt MyD88 self-association, we selected residues at the MyD88/MyD88 interface while leaving the MyD88/IRAK4 interface intact (Figure 2B). The MyD88 G80K mutation successfully disrupted aggregation as assayed by SEC (Figure 2A). Importantly, MyD88^{DD-G80K} retained the ability to assemble into a high molecular weight complex with dephosphorylated IRAK4^{FL} (Figure 2C).

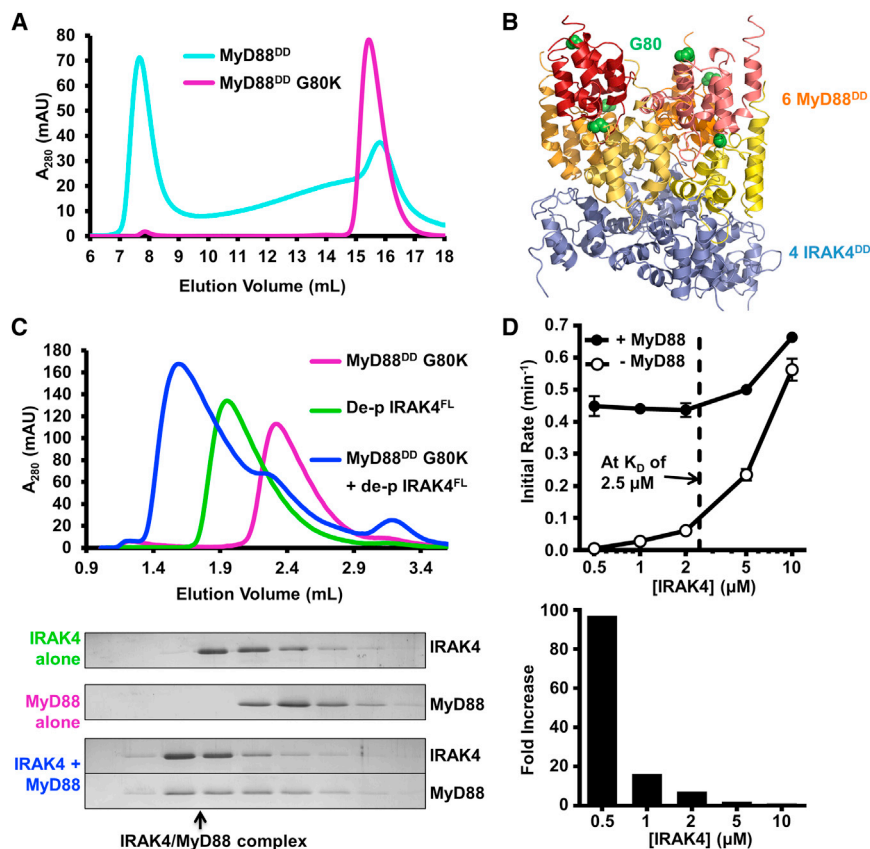


Figure 2. MyD88 Enhances IRAK4 *trans*-Autophosphorylation

(A) Size-exclusion chromatograms of MyD88^{DD} (cyan) and MyD88^{DD} with a solubilizing mutation (G80K, purple).

(B) Structure of the Myddosome DD complex containing MyD88^{DD} (warm colors) and IRAK4^{DD} (blue). Positions of MyD88 residue G80 are shown as green spheres.

(C) Size-exclusion chromatograms of MyD88^{DD} G80K (purple), dephosphorylated IRAK4^{FL} (green), and the IRAK4/MyD88 complex (blue) formed in vitro (top). SDS-PAGE of the fractions is shown with Coomassie blue staining (below). Black arrow indicates comigration of IRAK4 and MyD88 in a high molecular weight complex.

(D) Autophosphorylation rates of dephosphorylated IRAK4^{FL} at different concentrations, with (black circle) and without (open circle) pre-incubation with MyD88^{DD} G80K. Dotted black line indicates the K_D of IRAK4 dimerization. Data represent mean \pm SEM. Fold increase represents ratio of rates in the presence of MyD88 relative to those in the absence of MyD88.

See also Figure S2.

In order to understand the relationship between IRAK4 dimerization and activation, we performed autophosphorylation assays using [γ -³²P]ATP with different concentrations of dephosphorylated recombinant IRAK4^{FL} (Figure S2A). At high concentrations, IRAK4^{FL} efficiently underwent rapid autophosphorylation (Figure 2D). The rate of autophosphorylation was highly dependent on concentration. As the concentration of IRAK4^{FL} was lowered below that of the dimerization K_D , the rate of autophosphorylation decreased significantly (Figure 2D). At 500 nM, the rate of autophosphorylation is approximately 120-fold slower than that at 10 μ M. The correspondence between the concentration dependence of autophosphorylation and dimerization suggests that dimerization is a prerequisite for autophosphorylation.

Concentration-dependent autophosphorylation is indicative of *trans*-autophosphorylation rather than *cis*-autophosphorylation, as suggested previously from the inability of WT IRAK4 to phosphorylate a kinase-inactive mutant IRAK4^{FL-K213A/K214A} (Cheng et al., 2007). However, this experiment was performed at concentrations below 400 nM for WT and mutant IRAK4, which would exhibit a negligible rate shown in the concentration series of IRAK4 autophosphorylation (Figure 2D). In further support of *trans*-autophosphorylation, WT IRAK4^{FL} robustly phosphorylated the kinase-inactive mutant IRAK4^{KD-D311N} (Figure S2B, and see below).

Addition of MyD88^{DD-G80K} to the reaction resulted in dramatic increases of autophosphorylation rates (Figure 2D). At high concentrations, the effect of MyD88^{DD-G80K} was subtle, resulting in

a 1.2-fold increase at 10 μ M. The effect of rate acceleration of MyD88^{DD-G80K} was much more pronounced at low IRAK4^{FL} concentrations. At 500 nM IRAK4^{FL}, addition of MyD88^{DD-G80K} resulted in a near 100-fold increase in the autophosphorylation rate. The enhancement of IRAK4^{FL} autophosphorylation by MyD88 is dependent on the IRAK4 DD, as MyD88 did not interact with (Figure S2C) or promote the autophosphorylation of IRAK4^{KD} (Figure S2D). These data support the model in which kinase dimerization is required for efficient *trans*-autophosphorylation. Dimerization can be promoted either by increasing the kinase concentration above the dimerization K_D or by the incorporation of IRAK4 into the oligomeric Myddosome, effectively increasing the local concentration and promoting proximity-induced autophosphorylation. The linker between IRAK4 DD and KD contains approximately 57 residues; assuming an extended linker conformation, the lower limit of the local concentration of the kinase domain in the Myddosome would be \sim 150 μ M.

The Asymmetric Enzyme-Substrate Embrace in the IRAK4 Dimer Crystal Structure

We initially attempted crystallization of both IRAK4^{FL-D311N} alone and the IRAK4^{FL-D311N}/MyD88^{DD} complex (Figure S1A), with the former giving promising initial hits. However, SDS-PAGE analysis of the IRAK4^{FL-D311N} crystals revealed that they contained a fragment of IRAK4 that is consistent in molecular weight to the kinase domain (Figure S3A), suggesting that the protein had been proteolyzed in the linker between the DD and the KD during crystallization (Figure 1A). Given that Myddosome-induced dimerization and associated allosteric changes may be recapitulated in IRAK4^{KD-D311N} at the high protein concentration used in vitro, we pursued crystal optimization and structure determination of

Table 1. Crystallographic Statistics

	IRAK4 ^{KD-D311N} Native	IRAK4 ^{KD-D311N} Sulfur Anomalous
Constructs	Residues R164–S460	Residues R164–S460
Structure Determination	Molecular Replacement	Molecular Replacement
Data Collection		
Beamline	NLSL X29	NLSL X4A
Space group	P6 ₁ 22	P6 ₁ 22
Cell Dimensions		
a, b, c (Å)	87.6, 87.6, 421.6	87.5, 87.5, 424.0
Wavelength (Å)	1.075	2.0736
Resolution (Å)	41.81–2.65 (2.75–2.65)	38.88–2.80 (2.90–2.80)
CC1/2	1 (0.985)	0.999 (0.473)
R _{merge} (%)	12.1 (207)	18.3 (412)
Mean I/σ	37.2 (4.8)	45.8 (2.0)
Completeness (%)	100.0 (99.9)	97.3 (79.8)
Total Reflections	2,422,721 (244,494)	5,227,241 (94,043)
Unique Reflections	29,127 (2,830)	24,250 (1,929)
Redundancy	83.2 (86.4)	212.6 (62.4)
Refinement		
Resolution (Å)	41.81–2.65 (2.75–2.65)	38.88–2.80 (2.90–2.80)
R _{work} /R _{free} (%)	20.26/25.06	18.02/23.97
Number of Atoms	4,446	4,349
Proteins	4,264	4,264
Ligands	85	85
H ₂ O	97	0
Average B Factor (Å ²)	62.60	107.10
Proteins	63.20	107.20
Ligands	54.10	100.60
Rmsds		
Bond lengths (Å)/angles (°)	0.008/1.11	0.008/1.15
Ramachandran Plot		
Favored/outliers (%)	95/0	91/0.38

Numbers in parentheses are for the highest-resolution shell.

the IRAK4^{KD-D311N} dimer. Crystals of IRAK4^{KD-D311N} in complex with a pan-kinase inhibitor, the natural microbial alkaloid staurosporine, were obtained in space group P6₁22, a crystal form distinct from those of WT p-IRAK4^{KD} reported previously (Kuglstatter et al., 2007; Wang et al., 2006). The addition of staurosporine to IRAK4^{KD-D311N} does not induce dimerization and in fact may slightly inhibit dimer formation at low IRAK4^{KD-D311N} concentrations (Figure S3D). The structure was solved with molecular replacement and refined to a resolution of 2.65 Å (Table 1). The asymmetric unit contains two kinase monomers (A and B), each with staurosporine bound in the active site (Figure 3A).

Remarkably, the two IRAK4 monomers form an asymmetric dimer with a conformation resembling an “enzyme-substrate” embrace in which monomer A acts as the enzyme and monomer B acts as the substrate (Figure 3A). The enzyme monomer contains an ordered DFG motif and an activation loop conformation

similar to the p-IRAK4^{KD} structure in complex with staurosporine (Protein Data Bank [PDB] ID code 2NRY) (Figures 3B and S3B). Therefore, the enzyme monomer adopts a conformation typical of phosphorylated active IRAK4 without the prerequisite phosphorylation. Among the three phosphorylation sites of IRAK4, T345 is the prototypical phosphoresidue required for the active kinase conformation (Kuglstatter et al., 2007; Wang et al., 2006). Residue R334, which stabilizes the active conformation through its interaction with the phosphate of p-T345 in the p-IRAK4^{KD} structure (Kuglstatter et al., 2007; Wang et al., 2006), is disordered in the enzyme monomer of the IRAK4^{KD-D311N} structure (Figures 3B and S3B). The other two sites at T342 and S346 are nonprototypical sites of phosphorylation and do not make crucial intramolecular interactions for maintaining the active conformation in the crystal structures of p-IRAK4^{KD} (Kuglstatter et al., 2007; Wang et al., 2006).

Although the overall conformation of the substrate monomer in the asymmetric dimer is similar to the enzyme monomer with a root-mean-square deviation (rmsd) of 0.77 Å for 248 superimposed C α positions, part of the activation segment including the DFG motif and the activation loop showed striking differences (Figures 3C and S3C). In the substrate monomer, the activation loop is extended outward toward the active site of its partner, the enzyme monomer. Superposition of the enzyme monomer with the structure of phosphorylase kinase (PhK) bound to a peptide substrate shows a similarity in position and conformation between the PhK peptide substrate and the activation loop of the IRAK4 substrate monomer (Figure 3D), supporting the enzyme-substrate interpretation of the asymmetric IRAK4 dimer. Residues 348–350 of the enzyme monomer activation loop form an antiparallel β sheet with residues 346–348 of the substrate monomer activation loop (Figure 3E), consistent with the archetypal interactions involved in substrate recognition by protein kinases (Knighton et al., 1991).

Strikingly, T345 of the substrate monomer is positioned at the active site of the enzyme monomer, immediately adjacent to a bound sulfate ion in the crystal structure (Figure 3A). When AMP-PNP is modeled into the active site by superposition of the enzyme monomer with p-IRAK4 bound to the nucleotide (rmsd 0.30 Å) (PDB 2OID) (Kuglstatter et al., 2007), the γ -phosphate is located in approximately the same position as this sulfate (Figure 3F). Additionally, T345 of the substrate kinase makes hydrogen bonds with the catalytic base residue, here mutated to N311, as well as K313 and the sulfate ion (Figure 3A). K313 interacts with the sulfate ion in the same manner that it uses to stabilize the negative charge of the γ -phosphate of ATP. The mode of interaction of T345 with the catalytic base residue and a positively charged residue is similar to substrate recognition by the tyrosine kinases insulin receptor kinase (Hubbard, 1997) and insulin-like growth factor 1 receptor kinase (IGF1-RK) (Favelyukis et al., 2001). In the absence of Mg²⁺, the Mg²⁺ coordinating residue D329 instead forms water-mediated hydrogen bonds with the sulfate ion. Therefore, T345 is bound in a position and environment poised for the phosphotransfer reaction.

Because the residue preceding T345 is a Met (M344), we used sulfur anomalous diffraction to verify the correct placement of the substrate monomer activation loop. Highly redundant diffraction data were collected at 6 keV, where the calculated anomalous

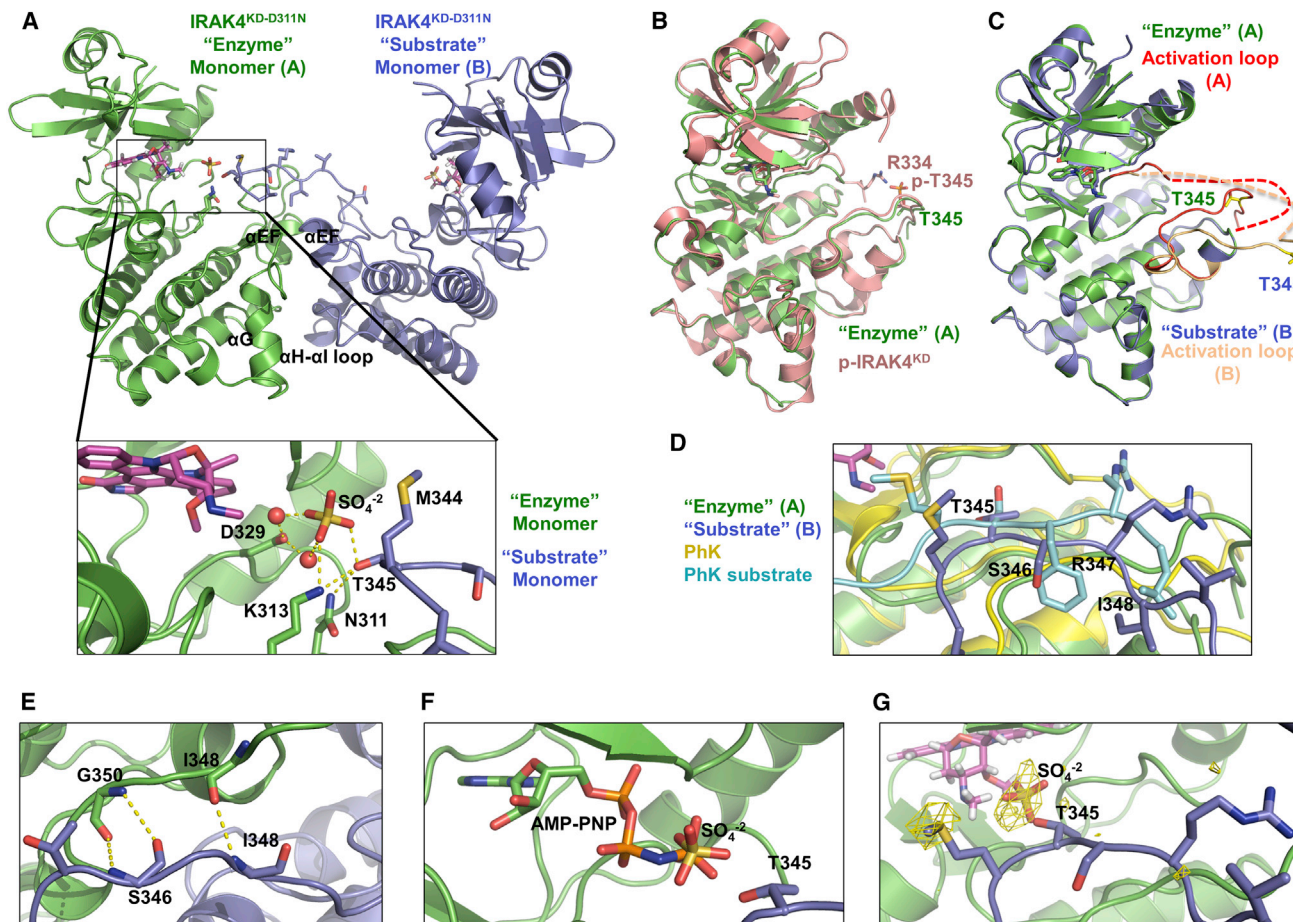


Figure 3. The Asymmetric Enzyme-Substrate Embrace in the IRAK4 Dimer Structure

(A) Ribbon diagram of IRAK4^{KD-D311N} dimer structure, shown in green for the enzyme monomer A and blue for the substrate monomer B. The pan-kinase inhibitor staurosporine (magenta), sulfate ion (red and yellow), enzyme monomer catalytic residues, and substrate monomer activation loop side chains are shown as sticks. Detailed interactions at the active site of the enzyme monomer are shown (inset). Hydrogen bonds are shown as dotted yellow lines. T345 is the prototypical phosphorylation residue.

(B) Superposition of IRAK4^{KD-D311N} enzyme monomer (green) with phosphorylated IRAK4^{KD} structure (p-IRAK4^{KD}, PDB: 2NRY) (pink).

(C) Superposition of IRAK4^{KD-D311N} enzyme monomer A (green) with substrate monomer B (blue). Monomer A activation loop (red) and monomer B activation loop (peach) adopt distinct conformations. Side chains of T345 are represented as yellow sticks to highlight differences in conformation.

(D) Superposition of IRAK4^{KD-D311N} enzyme monomer with phosphorylase kinase (PhK) (yellow) bound to a peptide substrate (teal) (PDB: 2PHK). Side chains of substrate monomer and PhK peptide are shown as sticks. Labels correspond to IRAK4^{KD-D311N} substrate monomer residues.

(E) Antiparallel hydrogen bonding interactions between IRAK4^{KD-D311N} enzyme monomer (green) and substrate monomer (blue).

(F) Modeled ATP analog AMP-PNP in the active site of IRAK4^{KD-D311N} enzyme monomer based on superposition with p-IRAK4^{KD}/AMP-PNP complex structure (PDB: 2OID). AMP-PNP, sulfate ion, and T345 of the substrate monomer are shown as sticks.

(G) Sulfur anomalous difference Fourier of IRAK4^{KD-D311N} structure contoured at 2.5 σ (yellow).

See also Table 1 and Figure S3.

scattering factor f'' is equal to 0.95 (Table 1). The structure was solved by molecular replacement, and peaks in the sulfur anomalous difference Fourier density were readily apparent. Importantly, the anomalous difference map showed the location of the sulfur atom in the side chain of M344, confirming that the assignment of the activation loop is correct (Figure 3G).

Symmetric, Exosite IRAK4 Dimerization at the C-Terminal Lobe

The IRAK4 dimer buries $\sim 1,160 \text{ \AA}^2$ surface area from each of the monomers, as calculated using the online program PDBePISA

(Krissinel and Henrick, 2007). In addition to the asymmetric activation loop interactions, the C-terminal lobes of the two kinases interact with each other at exosites across a noncrystallographic 2-fold symmetry axis (Figures 3A and 4A). The noncrystallographic 2-fold symmetry is almost perfect, with a 175.0° rotation between the two monomers. The C-terminal lobe contacts contain interactions between residues on helix α EF (the α EF exosite) and interactions between α G of one monomer and the α H- α I loop of the other monomer (the α G exosite) (Figure 4A). At the α EF exosite, residues L360 and R361 contribute large buried surface area through both hydrophobic and polar interactions

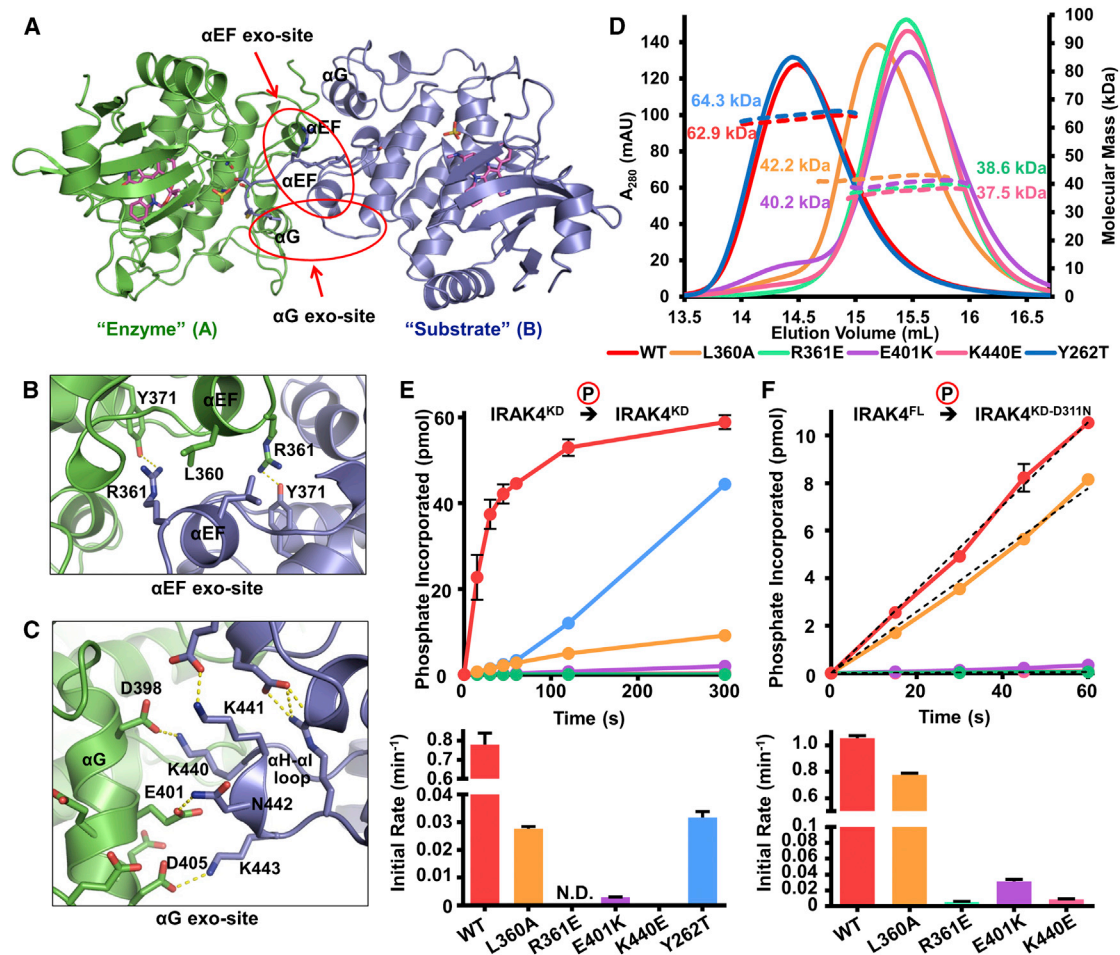


Figure 4. Symmetrical Exosite Interactions in IRAK4 Dimerization and Autophosphorylation

(A) Ribbon diagram of the IRAK4^{KD-D311N} dimer viewed down the approximate dimer axis, colored as in Figure 3A. Positions of the α G and α EF helices are indicated.

(B) Detailed interactions at the α EF exosite. Residues L360, R361, and Y371 of both monomers are labeled.

(C) Detailed interactions at the α G exosite. Side chains from negatively charged surface of α G and positively charged α H- α I loop are represented as sticks.

(D) Size-exclusion chromatograms (solid lines) and molecular masses as measured by MALS (dotted lines) of α EF exosite (L360A, R361E), α G exosite (E401K, K440E), and gatekeeper (Y262T) mutations on a IRAK4^{KD-D311N} background (WT).

(E) Autophosphorylation of 10 μ M IRAK4^{KD} (WT), IRAK4^{KD} with α EF exosite, α G exosite, and gatekeeper mutations as measured by autoradiography (top) and the initial rates of autophosphorylation (bottom). Data represent mean \pm SEM.

(F) *trans*-phosphorylation of IRAK4^{KD-D311N} with or without α EF exosite or α G exosite mutations (10 μ M) by IRAK4^{FL} (1 μ M) (top) and the initial rates of *trans*-phosphorylation (bottom). Data represent mean \pm SEM.

See also Figure S4.

(Figure 4B). The interaction at the α G exosite is highly charged, consisting of the acidic α G helix surface of one monomer and basic surface of the α H- α I loop on the opposing monomer (Figures 4C and S4A). As previously reported, helix α G exists in an unusual conformation, having swung out 10 Å away from α EF (Kuglstatter et al., 2007; Wang et al., 2006). This position of α G is unique to the IRAK4 kinase and is critical for the observed dimerization interface.

Analysis of residues at the dimerization interface indicates conservation among IRAK4 proteins from different species (Figure S4B), suggesting that IRAK4 dimerization is a general feature of its activation mechanism. There is no apparent sequence

similarity of the IRAK4 activation loop with a physiological IRAK4 substrate, the activation loop of IRAK1 (Hekmat-Nejad et al., 2010). This observation suggests that the IRAK4 activation loop is not an optimal IRAK4 substrate and that the exosite interactions are needed to facilitate IRAK4 *trans*-autophosphorylation.

Mutations that Disrupt IRAK4 Dimerization Inhibit Autophosphorylation In Vitro

To test the importance of the structurally observed IRAK4 dimer, we used mutagenesis to disrupt IRAK4 dimerization and studied the effects of mutations on IRAK4 autophosphorylation.

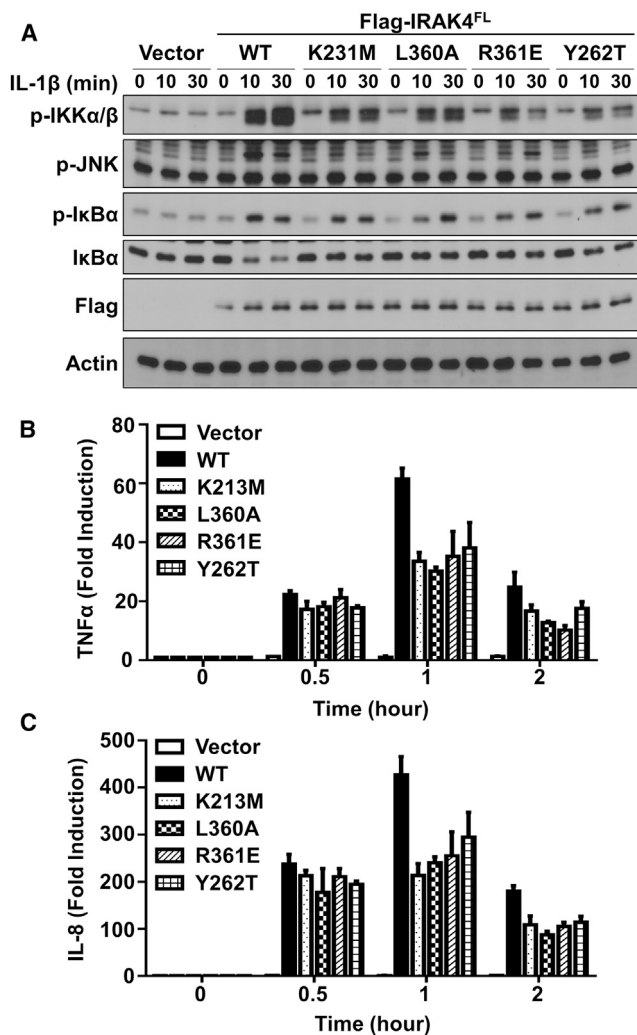


Figure 5. Disruption of IRAK4 Dimerization Results in Defective Signaling in Cells

(A) Human IRAK4-deficient fibroblasts infected with retroviruses containing empty vector construct (Vector), Flag-tagged IRAK4^{FL} wild-type (WT), and mutants (K213M, L360A, R361E, and Y262T) were treated with IL-1 β (1 ng/ml) for the indicated times, followed by western blot analyses using antibodies against p-IKK α/β , p-JNK, p-I κ B α , I κ B α , Flag, and actin.

(B and C) RT-PCR analyses for the fold induction of TNF- α (B) and IL-8 (C) expression in the same reconstituted human fibroblasts following treatment with IL-1 β for the indicated times. The experiment was repeated three times. Data represent mean \pm SEM.

See also Figure S5.

Residues L360 and R361 of the α EF helix, E401 of the α G helix, and K440 of the α H- α loop were targeted for mutagenesis based on their buried surface area and predicted contribution to the interface. These mutations were introduced into the dimeric IRAK4^{KD-D311N}. All selected mutations disrupted dimerization when analyzed by MALS (Figure 4D). The more conservative mutation, L360A, was less disruptive to dimerization than the charge reversal mutations and resulted in a less monomeric phenotype. These data confirmed the observed dimerization interface in the crystal.

Mutations that disrupt IRAK4 dimerization were then tested for their effect on IRAK4 autophosphorylation. The interface mutations were introduced into WT IRAK4^{KD}. Each kinase mutant was purified and dephosphorylated with λ -phosphatase. Autophosphorylation of these mutants was then assayed using [γ -³²P]ATP (Figure 4E). WT IRAK4^{KD} showed robust autophosphorylation. IRAK4^{KD-L360A} was partially defective, while the charge reversal mutations R361E, E401K, and K440E resulted in either extremely low or undetectable levels of autophosphorylation. The differential severity between the L360A and charge reversal autophosphorylation phenotypes corresponds with the partial and complete dimerization disruption observed in these mutants. In addition, we introduced these mutations into the inactive IRAK4^{KD-D311N} construct. They were then subjected to *trans*-phosphorylation by WT IRAK4^{FL} (Figure 4F). Robust *trans*-phosphorylation was detected when phosphorylating catalytically inactive IRAK4^{KD-D311N}. However the dimerization interface mutants showed attenuated phosphorylation by WT IRAK4, suggesting that disruption of dimerization impaired the ability of IRAK4 to act as a substrate. Again, the severity of the *trans*-autophosphorylation phenotypes correlated with the degree of dimerization disruption. The mutational effects on autophosphorylation (Figure 4E) are more severe than on *trans*-phosphorylation (Figure 4F), likely because in autophosphorylation the dimerization interfaces on both partners in the dimer are compromised. Taken together, these data demonstrate that dimerization is necessary for IRAK4 autophosphorylation.

Disruption of IRAK4 Dimerization Results in Defective Signaling in Cells

To test whether disruption of dimerization impairs the ability of IRAK4 to perform its role in signaling, we utilized an IRAK4-deficient human fibroblast cell line derived from a patient with recurrent pyogenic infections (Picard et al., 2003). These IRAK4-deficient human fibroblasts were reconstituted with either Flag-tagged WT human IRAK4^{FL}, the kinase-inactive mutant IRAK4^{FL-K213M}, IRAK4^{FL-L360A}, or IRAK4^{FL-R361E}. K213 is a critical ATP-binding residue at the N-terminal lobe, which is properly oriented for catalysis by an ion pair with the α C-helix conserved in all protein kinases (Nolen et al., 2004). These cells were then stimulated with IL-1 β , and the signaling properties were observed (Figure 5).

As reported previously, in comparison with IRAK4^{WT}, reconstitution with IRAK4^{FL-K213M} compromised IKK phosphorylation, I κ B α degradation, and JNK phosphorylation (Figure 5A) due to decreased TAK1-dependent IKK and MAP kinase activation (Fraczek et al., 2008; Yao et al., 2007). However, lack of IRAK4 kinase activity did not significantly affect I κ B α phosphorylation due to an alternative MEKK3-dependent pathway that phosphorylates but does not degrade I κ B α (Fraczek et al., 2008; Yao et al., 2007). Additionally, decreases in the levels of tumor necrosis factor alpha (TNF- α) and IL-8 mRNA were observed in the IRAK4^{FL-K213M} reconstituted cell line (Figures 5B and 5C). Remarkably, reconstitution with the dimerization-deficient mutants IRAK4^{FL-L360A} and IRAK4^{FL-R361E} resulted in phenotypes similar to those of kinase-inactive IRAK4^{FL-K213M} with respect to IKK and JNK phosphorylation, I κ B α degradation (Figure 5A), as well as TNF- α (Figure 5B) and IL-8 mRNA expression levels

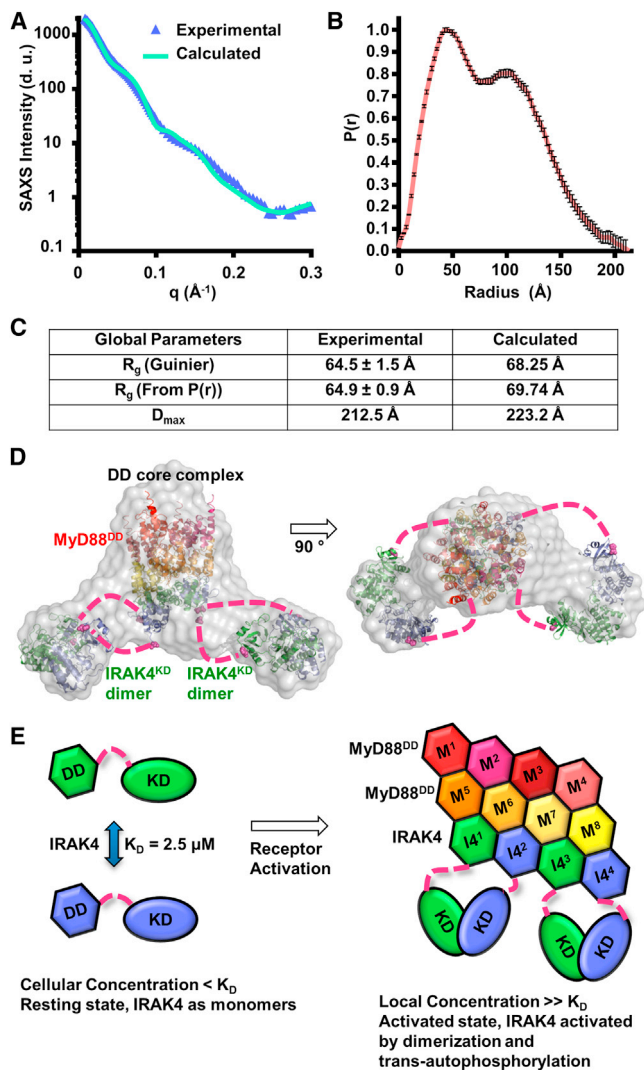


Figure 6. Small- and Wide-Angle X-Ray Scattering of the Myddosome

(A) Experimental scattering profile of the IRAK4^{FL-D311N}/MyD88^{DD} complex as a function of the scattering vector q ($q = 4\pi\sin(\theta/2)/\lambda$), where θ is the scattering angle and λ is the X-ray wavelength) after solvent background subtraction (blue), superimposed with the scattering profile calculated from the IRAK4^{FL-D311N}/MyD88^{DD} model in (D) (green). d.u., detector unit.

(B) Pair-distance distribution function ($P(r)$) of the IRAK4^{FL-D311N}/MyD88^{DD} complex. Data represent calculated $P(r)$ values \pm SD.

(C) Experimental and calculated radii of gyration (R_g) and maximum linear dimension (D_{\max}). Data represent calculated values \pm SD.

(D) The chevron-shaped molecular envelope (gray) from ab initio reconstruction fitted with structures of the binary Myddosome DD complex (PDB: 3MOP; 8 MyD88^{DD} in warm colors and 4 IRAK4^{DD} in green and blue) and 2 IRAK4^{KD} dimers (green and blue). The IRAK4 DDs and KDs presumed to be of the same polypeptides are shown in the same green or blue colors.

(E) Schematic model of IRAK4 dimerization and activation in the Myddosome in a signal-dependent manner.

(Figure 5C). Introduction of mutations into the IRAK4 kinase domain did not affect the interaction with MyD88 (Figure S5). These data demonstrate that IRAK4 dimerization is absolutely

required for IRAK4 kinase activation and the associated biological functions.

Small- and Wide-Angle X-Ray Scattering of the Myddosome

We next sought to obtain structural information on the Myddosome complex containing MyD88^{DD} and IRAK4^{FL} in order to understand the positioning of the kinase domains relative to the DD core. MyD88^{DD} was coexpressed with IRAK4^{FL-D311N} in insect cells. The complex was purified to homogeneity (Figure S1A) and subjected to SAXS/WAXS. Guinier analysis at low scattering angles indicated that the sample was free of aggregation (Figure 6A) and provided an estimated radius of gyration (R_g) of $64.5 \pm 1.5 \text{ \AA}$. The pair-distance distribution function ($P(r)$) obtained via indirect Fourier transformation possessed a bimodal shape (Figure 6B). The best $P(r)$ function was obtained with a maximum linear dimension (D_{\max}) of 212.5 \AA . The R_g of $64.9 \pm 0.9 \text{ \AA}$ obtained through indirect transform closely approximated the estimated value obtained with Guinier analysis (Figure 6C).

The $P(r)$ function obtained through indirect Fourier transform was then subjected to ab initio molecular envelope calculation. A total of 20 independent models were generated from different random seed starting points. Of the 20 initial models, 1 fell outside 2 SDs and was omitted from the ensemble. The 19 remaining models were averaged and filtered to an appropriate volume. The resulting envelope contained a central core flanked by two lobes on either side (Figure 6D). We reasoned that the envelope represented the central DD core of the Myddosome, flanked by two IRAK4 kinase dimers. Weaker densities were observed between the central core and the flanked lobes, suggesting the location of the linker between IRAK4 DD and KD. High-resolution crystal structures were modeled into this molecular envelope. In the docked model, the N-terminal lobes of the KD dimers face toward the core DD complex. The distances between C-terminal tails of IRAK4 DDs and N-terminal residues of KDs are between 48 \AA and 77 \AA , which can be easily accommodated by the linker of ~ 57 residues between the two domains. The docked model shows good agreement with experimental data (Figures 6A and 6C). Formation of IRAK4 KD dimers in the Myddosome supports proximity-driven dimerization and IRAK4 activation (Figure 6E).

Molecular Dynamics Simulations

Our mutagenesis data showed that the exosite interactions are crucial for IRAK4 dimer formation. However, direct mutagenesis of activation loop residues may lead to unforeseen effects on enzyme kinetics in addition to effects on the observed enzyme-substrate embrace. We thus turned to long-timescale MD simulations, which can reveal conformational changes on μs – ms timescales (Shaw et al., 2009). We first simulated the asymmetric IRAK4 dimer and verified its stability over the course of the MD simulation (Figures 7A and 7B). We then generated a hypothetical symmetrical dimer by replacing the substrate monomer with a superimposed enzyme monomer, effectively removing the asymmetric activation loop interaction while preserving symmetric exosite interactions. MD simulations of this symmetrical dimer resulted in rapid deviations in structure, which were much more substantial than those observed in the

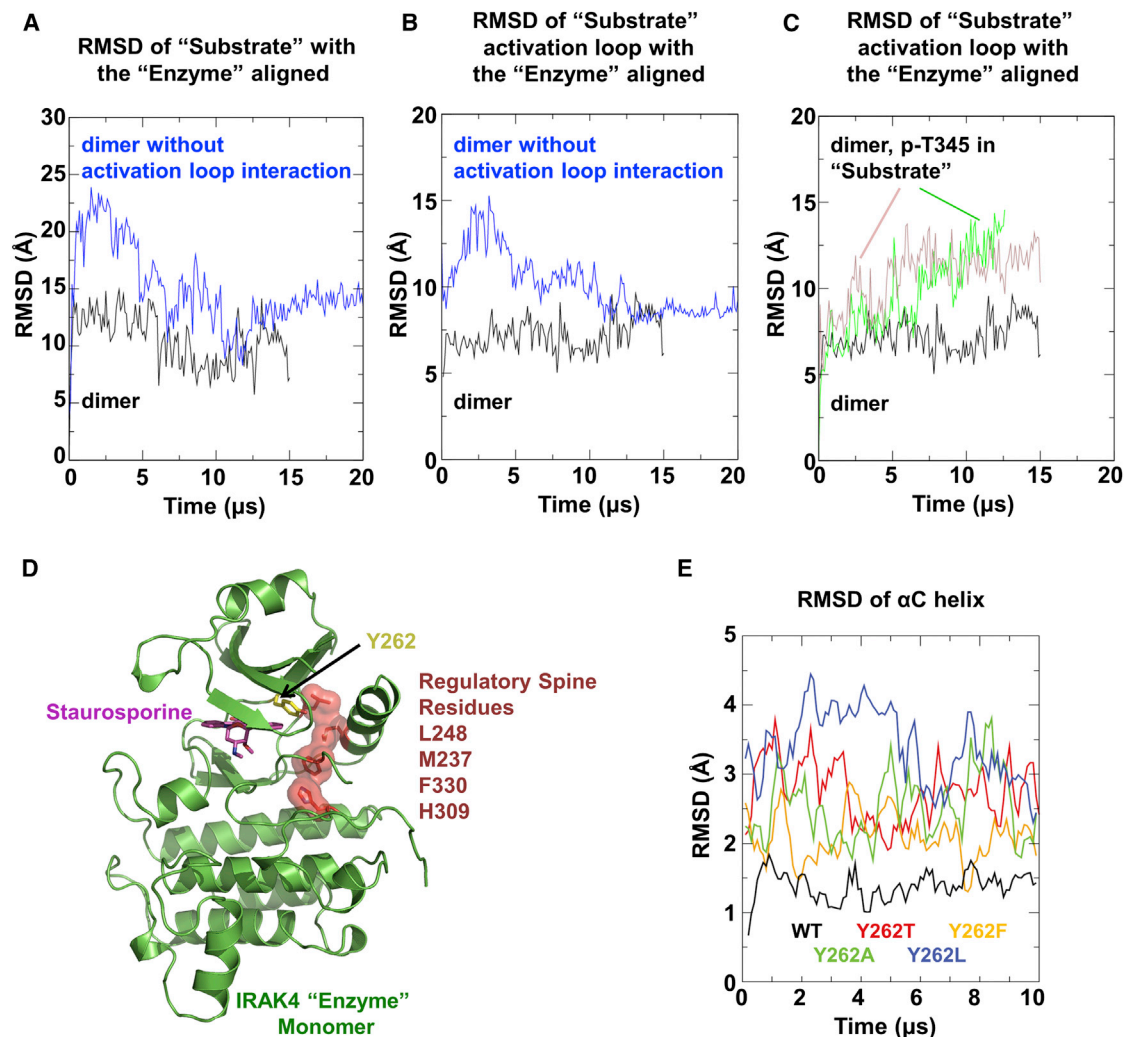


Figure 7. Molecular Dynamics Simulations

(A and B) MD simulation of the asymmetric IRAK4^{KD-D311N} dimer structure (black) and the hypothetical symmetrical dimer structure without activation loop interactions (blue). Rmsd values of C α atoms between the initial and simulated substrate monomer (A) or its activation loop (residue 329–354) (B) are shown when the enzyme monomer is aligned.

(C) MD simulation of the IRAK4^{KD-D311N} dimer structure hypothetically phosphorylated at T345 in the substrate monomer, with (pink) and without (green) bound ADP. Rmsd values of C α atoms between the initial and simulated substrate monomer activation loop are shown when the enzyme monomer is aligned.

(D) Ribbon diagram of enzyme monomer in the IRAK4^{KD-D311N} dimer structure, showing the regulatory spine residues (dark red) and the gatekeeper residue Y262 (yellow).

(E) MD simulation of the enzyme monomer with the hypothetical mutations in the gatekeeper tyrosine residue in comparison with WT (black). Rmsd values of C α atoms in the α C helix (residue 222–239) are shown when the initial and simulated structures are aligned with all C α atoms.

See also Figure S6.

asymmetric dimer simulations, suggesting that the activation loop interaction is important for maintaining the observed dimer configuration.

Our biochemical data established that activation loop phosphorylation dissociates IRAK4 dimers (Figure 1D). To deduce if T345, the canonical phosphorylation site in the activation loop of IRAK4, may be responsible for this dissociation, we simulated the stability of the enzyme-substrate-embraced dimer upon T345 phosphorylation. Consistent with our biochemical data, addition of the phosphate group to T345 induced large devia-

tions of the substrate kinase activation loop (Figure 7C), suggesting that dissociation would occur at longer timescales. These data provide evidence that phosphorylation at T345 is a mechanism of IRAK4 dimer dissociation.

DISCUSSION

Kinase activities are highly regulated, and in a large subset of kinases, this regulation is implemented by phosphorylation within the activation loop (Taylor and Kornev, 2011). In these

kinases, phosphorylated residues within the activation loop mediate specific intramolecular interactions that stabilize the active kinase conformation. For many kinases, this phosphorylation event is realized by *trans*-autophosphorylation between two identical kinase molecules, although examples of *cis*-autophosphorylation are also known (Hu et al., 2013).

We hypothesize that autophosphorylating kinases sample the active conformation more frequently than their nonautophosphorylating counterparts, even in the absence of activation loop phosphorylation. Protein kinases contain a highly conserved hydrophobic regulatory spine that anchors important elements for catalysis (Meharena et al., 2013; Taylor and Kornev, 2011). IRAK4 contains a unique gatekeeper residue Y262 (Kuglstatter et al., 2007; Wang et al., 2006), which packs against the regulatory spine (Figure 7D) and may stabilize the active conformation. In MD simulations, mutation of the unique Y262 to Ala or common gatekeeper residues, such as Thr, Phe, or Leu, led to destabilization of the active conformation in the absence of phosphorylation (Figure 7E). Additionally, IRAK4^{KD-Y262T} is defective for *in vitro* autophosphorylation (Figure 4E) without disrupting dimerization (Figure 4D), and reconstitution of IRAK4-deficient human fibroblasts with IRAK4^{FL-Y262T} does not restore WT signaling (Figure 5). Taken together, these data suggest that this unique tyrosine gatekeeper is critical for IRAK4's autophosphorylation activity.

Molecular mechanisms of *trans*-autophosphorylation have been pursued extensively. Structurally, analysis of crystal packing has revealed that several kinases known to autophosphorylate form activation-loop-swapped, symmetrical crystallographic dimers. These include the Ser/Thr kinase TBK1, important for interferon activation in innate immunity, the DNA damage checkpoint Ser/Thr kinase CHK2, and the tyrosine kinase IGF1-RK (Cai et al., 2009; Ma et al., 2012; Wu et al., 2008). Therefore, it has been proposed that reciprocal exchange of activation segments might be a common mechanism of *trans*-autophosphorylation (Oliver et al., 2007), which may explain the lack of sequence similarity between activation loops and substrates. However, because neither of the active sites is fully formed in these symmetrical dimers, it raises the question of how catalysis of *trans*-autophosphorylation is achieved in these conformations.

Formation of unphosphorylated IRAK4^{KD} dimers in solution gave us the unique opportunity to unambiguously correlate the dimer interface observed in the crystal with dimerization in solution, *trans*-autophosphorylation *in vitro* with and without MyD88, and signaling in cells. Our studies led to an elegant yet simple mechanism of *trans*-autophosphorylation in which one kinase assumes the active enzyme conformation while the partner kinase inserts its activation loop as a substrate. Curiously, the exosite interactions in the IRAK4 dimer represent a commonly used allosteric site (Goldsmith et al., 2007) and likely further promote adoption of an active conformation of the enzyme kinase. For example, a similar exosite containing the α G helix is used in recognition of the substrate eIF2 α by protein kinase RNA-activated (PKR) (Seo et al., 2008) (Figure S6A). The modest dimerization constant renders IRAK4 in an inactive state at physiological concentrations and safeguards against spontaneous ligand-independent autoactivation. Recruitment of IRAK4 to MyD88 to form the Myddo-

some dramatically increases the local concentration of IRAK4, promoting dimerization and allosteric activation (Figure 6E). Addressing allosteric changes responsible for enzyme activation in oligomerization-driven biological systems remains an important and exciting challenge for structural biologists.

The mode of *trans*-autophosphorylation elucidated here has been proposed previously for p21-activated kinases (PAKs) (Pirruccello et al., 2006). The active conformation of IRAK4 in the absence of phosphorylation is reminiscent of PAK1, which showed an active conformation without the cognate Thr phosphorylation (Lei et al., 2005). An asymmetric enzyme-substrate dimer was also observed in the crystal lattice of the unphosphorylated PAK1 structure (Wang et al., 2011) (Figure S6B), which suggests a common mechanism of *trans*-autophosphorylation. Unlike the IRAK4 dimer, the exosite interactions in the PAK1 dimer are not symmetrical. In both cases, the extensive exosite interactions may facilitate the positioning of the activation loops as substrates, explaining the lack of sequence similarity between activation loops and substrates. Given the highly dynamic nature of protein kinases, it is likely that a variety of different structural features are utilized to achieve autophosphorylation.

EXPERIMENTAL PROCEDURES

Cloning and Protein Purification

Human IRAK4, FL, KD, and all mutants were expressed in insect cells, while MyD88^{DD} MyD88^{DD-G80K} and IRAK4^{DD} were expressed in *E. coli*. Proteins were purified with HisPur Cobalt Resin (Thermo Scientific) followed by anion exchange and size-exclusion chromatography (Superdex 200 10/300 GL, GE Healthcare).

Multangle Light Scattering

Samples were applied over a Superdex 200 10/300 GL column coupled to a three-angle light scattering detector (mini-DAWN TRISTAR) and a refractive index detector (Optilab DSP) (Wyatt Technology).

Sedimentation Equilibrium Analytical Ultracentrifugation

IRAK4^{FL-D311N} was subjected to ultracentrifugation until equilibrium was reached in a Beckman Coulter Optima XL-A ultracentrifuge with an An-60 Ti rotor using six-channel centerpieces and quartz glass.

Crystallization, Data Collection, and Structure Determination

IRAK4^{KD-D311N} was cocrystallized with staurosporine in 1.6–1.9 M ammonium sulfate and 100 mM HEPES-NaOH (pH 7). Crystals were cryoprotected and flash frozen in liquid nitrogen. Data collection was performed at the National Synchrotron Light Source (NSLS).

Kinase Assays

Dephosphorylated IRAK4 was subjected to auto- and *trans*-phosphorylation experiments with or without precubation with MyD88^{DD-G80K} using [γ -³²P] ATP. Phosphoproteins were separated from free nucleotides by SDS-PAGE and visualized by autoradiography.

Plasmids and Retroviruses

IRAK4 WT and mutants were cloned into pMXs-IRES-Puro and transfected into Phoenix cells for viral packaging. Human IRAK4-deficient fibroblasts were infected by the packaged retrovirus, and stable viral integration was selected by puromycin.

Immunoblotting and Coimmunoprecipitation

Cell lysates were separated by 10% SDS-PAGE, transferred to Immobilon-P membranes (Millipore), and subjected to immunoblotting. For

coimmunoprecipitations, cell lysates were incubated with 20 μ l of protein A-Sepharose beads with anti-Flag antibody before immunoblotting.

Quantitative Real-Time PCR

Total RNA was isolated using TRIzol reagent (Invitrogen) and subjected to reverse transcription using SuperScript-reverse transcriptase (Invitrogen). Quantitative PCR was performed on an AB 7300 RealTime PCR System.

Small- and Wide-Angle X-Ray Scattering

Data were collected in triplicate on the IRAK4^{FL-D311N}/MyD88^{DD} complex at concentrations of 2, 1, and 0.5 mg/ml. Data were merged and scaled, followed by evaluation of the particle distance distribution function $P(r)$ and ab initio modeling.

Molecular Dynamics Simulations

Equilibrium molecular dynamics simulations were performed on the special-purpose molecular dynamics machine Anton (Shaw et al., 2009).

ACCESSION NUMBERS

The accession numbers for the data reported in this paper are 4U97 and 4U9A.

SUPPLEMENTAL INFORMATION

Supplemental Information includes Supplemental Experimental Procedures and six figures and can be found with this article online at <http://dx.doi.org/10.1016/j.molcel.2014.08.006>.

AUTHOR CONTRIBUTIONS

R.F. performed protein purification, SEC, MALS, AUC, in vitro kinase assays, crystallization, structure determination, and SAXS, including Figures 1, 2, 3, 4, 6, S1, S2, S3, S4, and S6. H.Z. performed and X.L. oversaw cellular signaling analyses, western blots, RT-PCR, and coimmunoprecipitation, including Figures 5 and S5. Y.S. performed MD simulations, including Figure 7. Q. Liu collected and processed sulfur anomalous data. Q. Li expressed protein in insect cells. H.W. supervised the project. R.F., H.W., H.Z., Y.S., and X.L. wrote the manuscript.

ACKNOWLEDGMENTS

We thank Dr. Wayne Hendrickson for suggesting the use of X4A beamline of NSLS for sulfur anomalous diffraction, Dr. Venkatesh Mysore for assistance in performing the MD simulation, Dr. Stewart Shuman and Dr. Heather Ordonez for their technical support and advice involving radiolabeled kinase assays, Dr. Stephen Harrison and Dr. Yoana Dimitrova for access to the SE-AUC equipment and assistance with the experiment, and the National Institutes of Health for funding support (AI050872 to H.W.).

Received: March 3, 2014

Revised: June 23, 2014

Accepted: July 31, 2014

Published: September 4, 2014

REFERENCES

Cai, Z., Chehab, N.H., and Pavletich, N.P. (2009). Structure and activation mechanism of the CHK2 DNA damage checkpoint kinase. *Mol. Cell* 35, 818–829.

Cheng, H., Addona, T., Keshishian, H., Dahlstrand, E., Lu, C., Dorsch, M., Li, Z., Wang, A., Ocain, T.D., Li, P., et al. (2007). Regulation of IRAK-4 kinase activity via autophosphorylation within its activation loop. *Biochem. Biophys. Res. Commun.* 352, 609–616.

Favelyukis, S., Till, J.H., Hubbard, S.R., and Miller, W.T. (2001). Structure and autoregulation of the insulin-like growth factor 1 receptor kinase. *Nat. Struct. Biol.* 8, 1058–1063.

Ferrao, R., and Wu, H. (2012). Helical assembly in the death domain (DD) superfamily. *Curr. Opin. Struct. Biol.* 22, 241–247.

Ferrao, R., Li, J., Bergamin, E., and Wu, H. (2012). Structural insights into the assembly of large oligomeric signalosomes in the Toll-like receptor-interleukin-1 receptor superfamily. *Sci. Signal.* 5, re3.

Fraczek, J., Kim, T.W., Xiao, H., Yao, J., Wen, Q., Li, Y., Casanova, J.L., Pryjma, J., and Li, X. (2008). The kinase activity of IL-1 receptor-associated kinase 4 is required for interleukin-1 receptor/toll-like receptor-induced TAK1-dependent NF κ B activation. *J. Biol. Chem.* 283, 31697–31705.

Goldsmith, E.J., Akella, R., Min, X., Zhou, T., and Humphreys, J.M. (2007). Substrate and docking interactions in serine/threonine protein kinases. *Chem. Rev.* 107, 5065–5081.

Hekmat-Nejad, M., Cai, T., and Swinney, D.C. (2010). Steady-state kinetic characterization of kinase activity and requirements for Mg²⁺ of interleukin-1 receptor-associated kinase-4. *Biochemistry* 49, 1495–1506.

Hu, J., Stites, E.C., Yu, H., Germino, E.A., Meharena, H.S., Stork, P.J., Kornev, A.P., Taylor, S.S., and Shaw, A.S. (2013). Allosteric activation of functionally asymmetric RAF kinase dimers. *Cell* 154, 1036–1046.

Hubbard, S.R. (1997). Crystal structure of the activated insulin receptor tyrosine kinase in complex with peptide substrate and ATP analog. *EMBO J.* 16, 5572–5581.

Jin, M.S., and Lee, J.O. (2008). Structures of TLR-ligand complexes. *Curr. Opin. Immunol.* 20, 414–419.

Kawai, T., and Akira, S. (2010). The role of pattern-recognition receptors in innate immunity: update on Toll-like receptors. *Nat. Immunol.* 11, 373–384.

Knighton, D.R., Zheng, J.H., Ten Eyck, L.F., Xuong, N.H., Taylor, S.S., and Sowadski, J.M. (1991). Structure of a peptide inhibitor bound to the catalytic subunit of cyclic adenosine monophosphate-dependent protein kinase. *Science* 253, 414–420.

Krissinel, E., and Henrick, K. (2007). Inference of macromolecular assemblies from crystalline state. *J. Mol. Biol.* 372, 774–797.

Kuglstatter, A., Villaseñor, A.G., Shaw, D., Lee, S.W., Tsing, S., Niu, L., Song, K.W., Barnett, J.W., and Browner, M.F. (2007). Cutting Edge: IL-1 receptor-associated kinase 4 structures reveal novel features and multiple conformations. *J. Immunol.* 178, 2641–2645.

Lei, M., Robinson, M.A., and Harrison, S.C. (2005). The active conformation of the PAK1 kinase domain. *Structure* 13, 769–778.

Li, S., Strelow, A., Fontana, E.J., and Wesche, H. (2002). IRAK-4: a novel member of the IRAK family with the properties of an IRAK-kinase. *Proc. Natl. Acad. Sci. USA* 99, 5567–5572.

Lin, S.C., Lo, Y.C., and Wu, H. (2010). Helical assembly in the MyD88-IRAK4-IRAK2 complex in TLR/IL-1R signalling. *Nature* 465, 885–890.

Ma, X., Helgason, E., Phung, Q.T., Quan, C.L., Iyer, R.S., Lee, M.W., Bowman, K.K., Starovastnik, M.A., and Dueber, E.C. (2012). Molecular basis of Tank-binding kinase 1 activation by transautophosphorylation. *Proc. Natl. Acad. Sci. USA* 109, 9378–9383.

Meharena, H.S., Chang, P., Keshwani, M.M., Oruganty, K., Nene, A.K., Kannan, N., Taylor, S.S., and Kornev, A.P. (2013). Deciphering the structural basis of eukaryotic protein kinase regulation. *PLoS Biol.* 11, e1001680.

Motshwene, P.G., Moncrieffe, M.C., Grossmann, J.G., Kao, C., Ayalaru, M., Sandercock, A.M., Robinson, C.V., Latz, E., and Gay, N.J. (2009). An oligomeric signaling platform formed by the Toll-like receptor signal transducers MyD88 and IRAK-4. *J. Biol. Chem.* 284, 25404–25411.

Netea, M.G., Wijmenga, C., and O'Neill, L.A. (2012). Genetic variation in Toll-like receptors and disease susceptibility. *Nat. Immunol.* 13, 535–542.

Ngo, V.N., Young, R.M., Schmitz, R., Jhavar, S., Xiao, W., Lim, K.H., Kohlhammer, H., Xu, W., Yang, Y., Zhao, H., et al. (2011). Oncogenically active MYD88 mutations in human lymphoma. *Nature* 470, 115–119.

Nolen, B., Taylor, S., and Ghosh, G. (2004). Regulation of protein kinases; controlling activity through activation segment conformation. *Mol. Cell* 15, 661–675.

- Oliver, A.W., Knapp, S., and Pearl, L.H. (2007). Activation segment exchange: a common mechanism of kinase autophosphorylation? *Trends Biochem. Sci.* *32*, 351–356.
- Pellicena, P., and Kuriyan, J. (2006). Protein-protein interactions in the allosteric regulation of protein kinases. *Curr. Opin. Struct. Biol.* *16*, 702–709.
- Picard, C., Puel, A., Bonnet, M., Ku, C.L., Bustamante, J., Yang, K., Soudais, C., Dupuis, S., Feinberg, J., Fieschi, C., et al. (2003). Pyogenic bacterial infections in humans with IRAK-4 deficiency. *Science* *299*, 2076–2079.
- Pirruccello, M., Sondermann, H., Pelton, J.G., Pellicena, P., Hoelz, A., Chernoff, J., Wemmer, D.E., and Kuriyan, J. (2006). A dimeric kinase assembly underlying autophosphorylation in the p21 activated kinases. *J. Mol. Biol.* *361*, 312–326.
- Seo, E.J., Liu, F., Kawagishi-Kobayashi, M., Ung, T.L., Cao, C., Dar, A.C., Sicheri, F., and Dever, T.E. (2008). Protein kinase PKR mutants resistant to the poxvirus pseudosubstrate K3L protein. *Proc. Natl. Acad. Sci. USA* *105*, 16894–16899.
- Shaw, D.E., Dror, R.O., Salmon, J.K., Grossman, J.P., Mackenzie, K.M., Bank, J.A., Young, C., Deneroff, M.M., Batson, B., Bowers, K.J., et al. (2009). Millisecond-scale molecular dynamics simulations on Anton. In *Proceedings of the Conference on High Performance Computing Networking, Storage and Analysis* (Portland, Oregon: ACM), pp. 1–11.
- Taylor, S.S., and Kornev, A.P. (2011). Protein kinases: evolution of dynamic regulatory proteins. *Trends Biochem. Sci.* *36*, 65–77.
- Thomas, C., Bazan, J.F., and Garcia, K.C. (2012). Structure of the activating IL-1 receptor signaling complex. *Nat. Struct. Mol. Biol.* *19*, 455–457.
- Treon, S.P., Xu, L., Yang, G., Zhou, Y., Liu, X., Cao, Y., Sheehy, P., Manning, R.J., Patterson, C.J., Tripsas, C., et al. (2012). MYD88 L265P somatic mutation in Waldenström's macroglobulinemia. *N. Engl. J. Med.* *367*, 826–833.
- von Bernuth, H., Picard, C., Jin, Z., Pankla, R., Xiao, H., Ku, C.L., Chrabieh, M., Mustapha, I.B., Ghandil, P., Camcioglu, Y., et al. (2008). Pyogenic bacterial infections in humans with MyD88 deficiency. *Science* *321*, 691–696.
- Wang, Z., Liu, J., Sodom, A., Ayres, M., Li, S., Wesche, H., Powers, J.P., and Walker, N.P. (2006). Crystal structures of IRAK-4 kinase in complex with inhibitors: a serine/threonine kinase with tyrosine as a gatekeeper. *Structure* *14*, 1835–1844.
- Wang, D., Zhang, S., Li, L., Liu, X., Mei, K., and Wang, X. (2010). Structural insights into the assembly and activation of IL-1 β with its receptors. *Nat. Immunol.* *11*, 905–911.
- Wang, J., Wu, J.W., and Wang, Z.X. (2011). Structural insights into the autoactivation mechanism of p21-activated protein kinase. *Structure* *19*, 1752–1761.
- Wu, H. (2013). Higher-order assemblies in a new paradigm of signal transduction. *Cell* *153*, 287–292.
- Wu, J., Li, W., Craddock, B.P., Foreman, K.W., Mulvihill, M.J., Ji, Q.S., Miller, W.T., and Hubbard, S.R. (2008). Small-molecule inhibition and activation-loop trans-phosphorylation of the IGF1 receptor. *EMBO J.* *27*, 1985–1994.
- Yao, J., Kim, T.W., Qin, J., Jiang, Z., Qian, Y., Xiao, H., Lu, Y., Qian, W., Gulen, M.F., Sizemore, N., et al. (2007). Interleukin-1 (IL-1)-induced TAK1-dependent Versus MEKK3-dependent NFkappaB activation pathways bifurcate at IL-1 receptor-associated kinase modification. *J. Biol. Chem.* *282*, 6075–6089.

Molecular Cell, Volume 55

Supplemental Information

IRAK4 Dimerization and *trans*-Autophosphorylation Are Induced by Myddosome Assembly

Ryan Ferrao, Hao Zhou, Yibing Shan, Qun Liu, Qiubai Li, David E. Shaw, Xiaoxia Li, and Hao Wu

SUPPLEMENTAL FIGURES

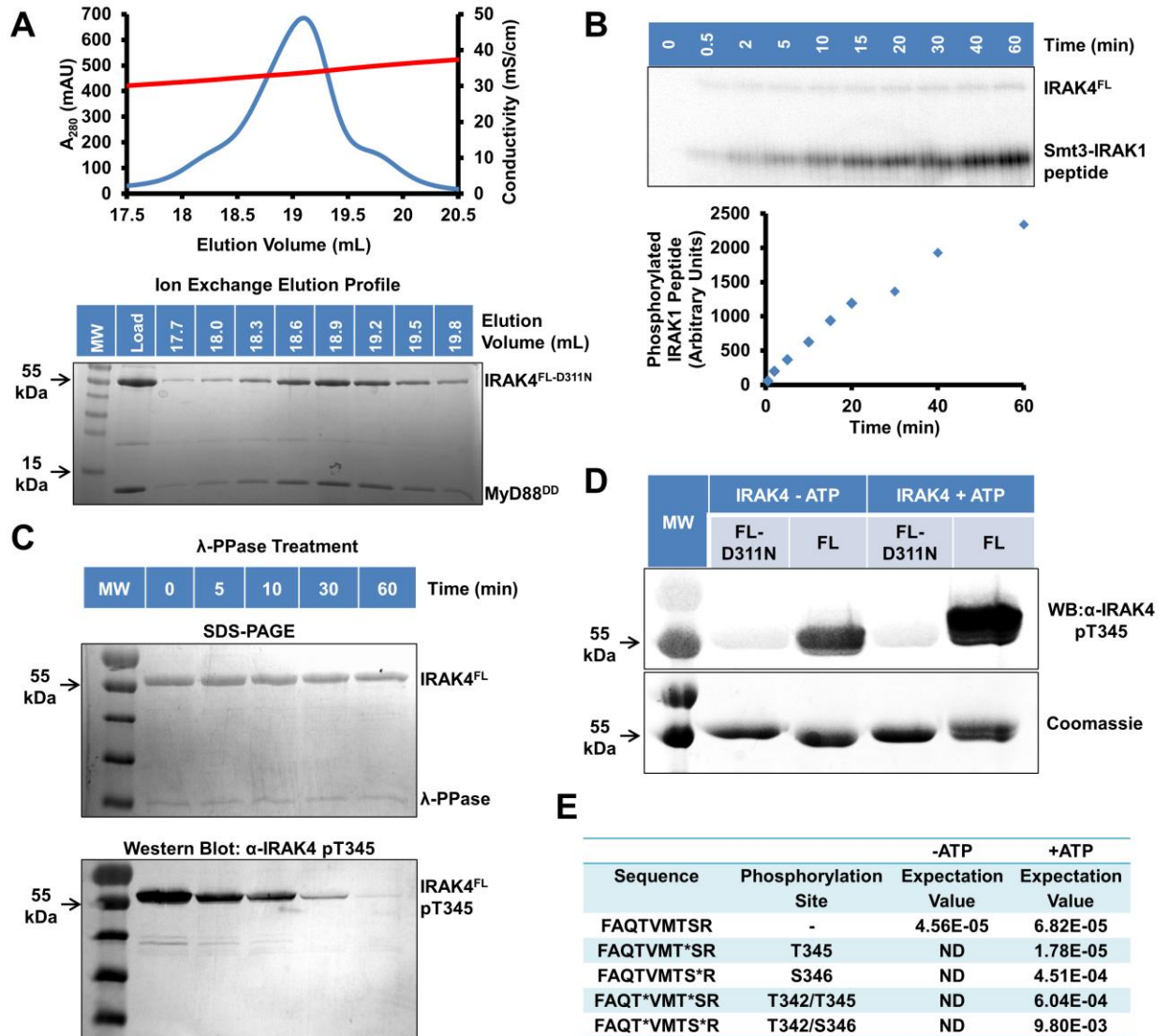


Figure S1. Characterization of IRAK4 Activity and Phosphorylation State, Related to Figure 1

- (A) Anion-exchange chromatography of co-expressed IRAK4^{FL-D311N}/MyD88^{DD} complex. A₂₈₀ absorption profile (blue) shows major elution peak at a conductivity of approximately 35 mS/cm (red). SDS-PAGE of anion-exchange fractions followed by Coomassie blue staining indicates that the peak contains both IRAK4^{FL-D311N} and MyD88^{DD}.
- (B) Phosphorylation of 160 μM Smt3 tagged IRAK1 activation loop peptide (362-380) by 300 nM IRAK4^{FL}. Samples at various time points were separated by SDS-PAGE, visualized by autoradiography (top) and quantified (bottom).
- (C) Dephosphorylation of IRAK4^{FL}. Natively phosphorylated IRAK4^{FL} was incubated with λ-phosphatase at 30 °C. Samples at various time points were analyzed by SDS-PAGE

followed by either Coomassie blue staining (top) or Western blot using a phospho-specific antibody for IRAK4 pT345 (bottom).

- (D) Phosphorylation of insect cell purified IRAK4^{FL} and IRAK4^{FL-D311N} examined before and after incubation with 5 mM ATP at 25 °C. Samples were separated by SDS-PAGE and visualized by anti-IRAK4 pT345 Western blot (top) and Coomassie blue staining (bottom).
- (E) Liquid Chromatography Tandem Mass Spectrometry (LC-MS/MS) of λ -phosphatase treated IRAK4^{FL}, with and without incubation with ATP/Mg²⁺. Shown are the significant phosphorylation events on the IRAK4 activation loop residues, T342, T345, and S346, along with the expectation value of each ion.

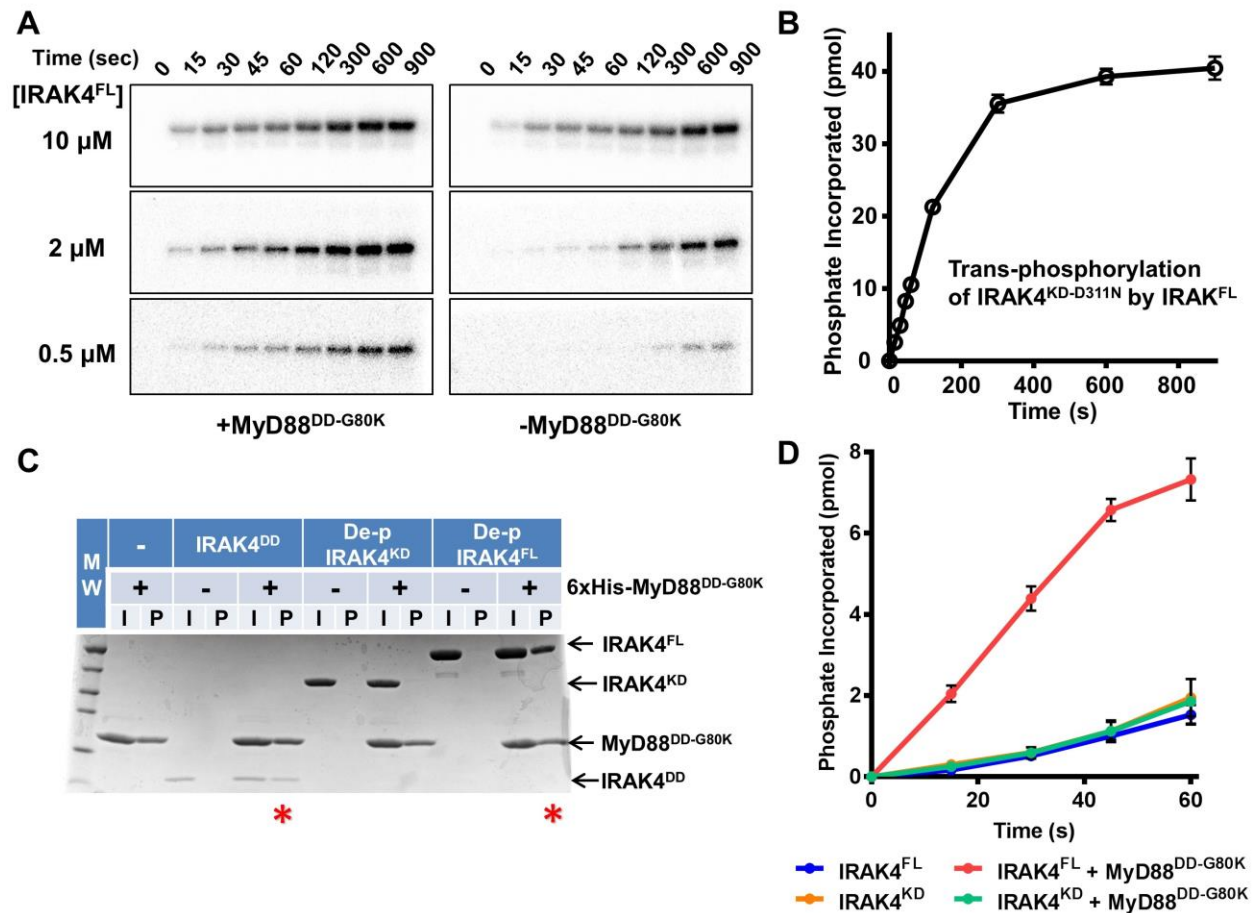


Figure S2. MyD88 Enhances *Trans*-autophosphorylation of IRAK4, Related to Figure 2

- (A) Representative autoradiography images of IRAK4^{FL} autophosphorylation with and without MyD88^{DD-G80K}. IRAK4^{FL} samples at indicated concentrations were incubated with [γ -³²P]ATP and Mg²⁺ at 25 °C. IRAK4^{FL} was pre-incubated with or without MyD88^{DD-G80K}. Timepoints were subjected to SDS-PAGE and visualized by autoradiography.
- (B) *Trans*-phosphorylation of IRAK4^{KD-D311N} (10 μM) by IRAK4^{FL} (1 μM). The same data is shown as part of Figure 4F. Data represent mean ± SEM.
- (C) Pull-down assay of 100 μM 6xHis tagged MyD88^{DD-G80K} with 25 μM dephosphorylated IRAK4^{DD}, IRAK4^{KD}, or IRAK4^{FL}. Red asterisks indicate successful pull-down of IRAK4 construct. I: input, P: pulldown.
- (D) Autophosphorylation of 2 μM dephosphorylated IRAK4^{FL} or IRAK4^{KD} with and without 50 μM MyD88^{DD-G80K} preincubation. Data represent mean ± SEM.

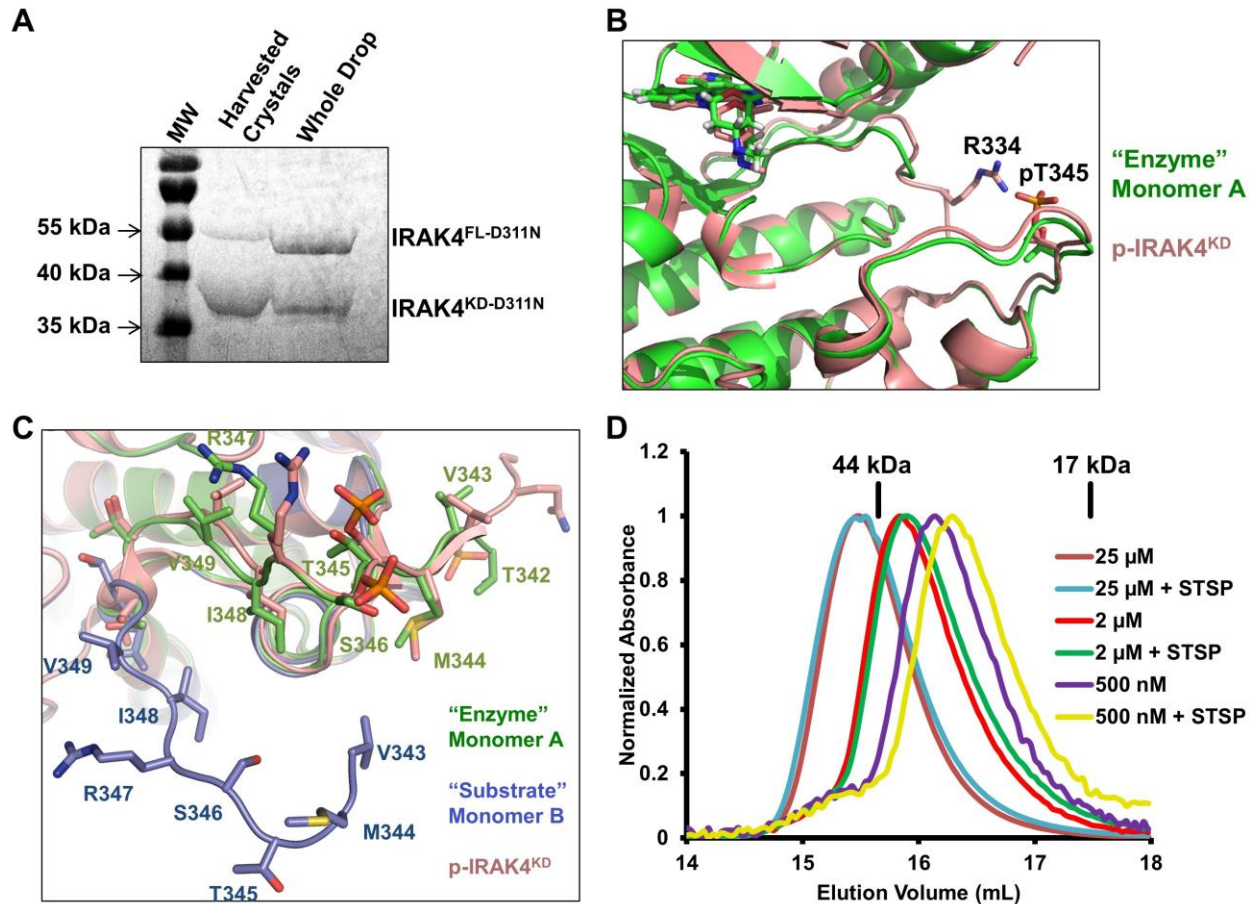
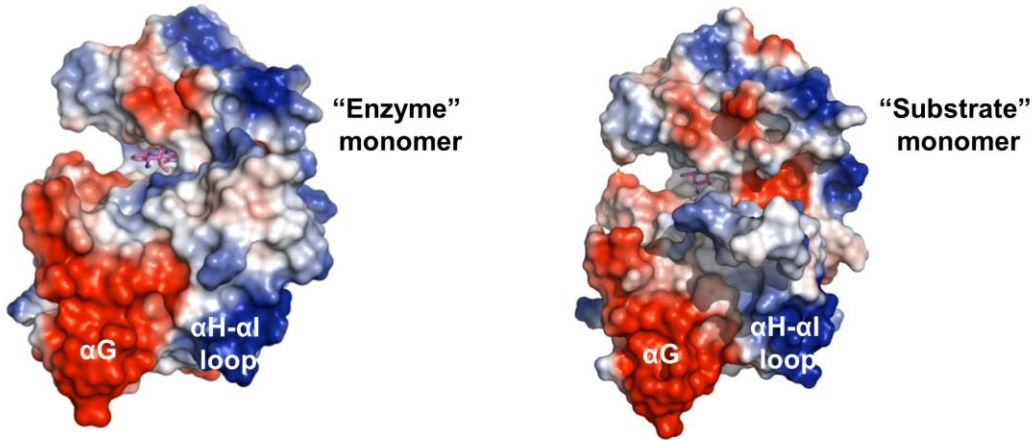


Figure S3. Activation Loop of Each IRAK4 Monomer Adopts a Distinct Conformation, Related to Figure 3

- (A) Coomassie stained SDS-PAGE of IRAK4^{FL-D311N} crystals and the crystallization drop. Several crystals were harvested and washed with reservoir solution before addition of SDS-PAGE loading buffer (Harvested Crystals). This was compared to the protein composition of the complete drop (Whole Drop), indicating that the crystals are enriched for the IRAK4 degradation product that is consistent in molecular weight with the IRAK4 kinase domain.
- (B) Superposition of IRAK4^{KD-D311N} “enzyme” monomer A with p-IRAK4^{KD} as in Figure 3B. The canonical phosphorylated residue, pT345 of p-IRAK4^{KD} and T345 of IRAK4^{KD-D311N} are shown as sticks. R334 of p-IRAK4^{KD} forms a salt bridge with the phosphate group of pT345, but is disordered in the structure of IRAK4^{KD-D311N}.
- (C) Superposition of IRAK4^{KD-D311N} “enzyme” monomer A, “substrate” monomer B, and p-IRAK4^{KD}. The activation loop conformation of IRAK4^{KD-D311N} “substrate” monomer B is distinct from that of IRAK4^{KD-D311N} “enzyme” monomer A and p-IRAK4^{KD}. Activation loop residue side chains are shown as sticks and labeled for the IRAK4^{FL-D311N} structure.
- (D) Normalized size-exclusion chromatograms of IRAK4^{KD-D311N} at indicated concentrations incubated with either DMSO or 500 μM staurosporine.

A



B

	ACTIVATION LOOP	α EF HELIX	α G HELIX	α H- α I LOOP				
Human IRAK4	166	HSFSFYELKNVTNNFDERPISVGGNKMGE	GGFGVVYKGYVNN	TTVAVKKLAAMVDITTEE	225			
Bovine IRAK4	HSFSFFELKDVTNNFDERPISVGGNKMGE	GGFGVVYKGYVNN	TTVAVKKLAAMVDISTEE					
Mouse IRAK4	HSFSFHLEKSI	TNNFDEQ	PASAGGNRMGE	GGFGVVYKGCVNN	TTVAVKKLGAMVEISTEE			
Xenopus IRAK4	GRFSFTEVKQSTNNFDIRPVSEGGNKLGE	GGFGVVFKGEI	KEKIVAVKKL	TELVDASIQD				
Zebrafish IRAK4	HTFSLHELTAMTQH	WDERPLSDGGCRLG	SGGFGVVFRGRMGDKH	VAVKKLNPLDGSSYED				
Human IRAK4	226	LKQOFDQEI	KVMAKCOHENLV	ELLGFSSDGD	DDCLVYVYMPNGS	LLDRLSCLDGT	PPPSW	285
Bovine IRAK4	LKQOFDQEI	KVMAKCOHENLV	ELLGFSSDGD	DDCLVYVYMPNGS	LLDRLSCLDGT	PPPSW		
Mouse IRAK4	LKQOFDQEI	KVMATCOHENLV	ELLGFSSDSD	NDCLVYAYMPNGS	LLDRLSCLDGT	PPPSW		
Xenopus IRAK4	LTCQFEQEI	KIMGKCOHENLV	KLLGYSKDGD	QYCLITYYMPNGS	LLDRLACLND	TPPI	SW	
Zebrafish IRAK4	LRKQFNQEI	QTLRSLSHEN	VLRLVLCSCSGP	PLCVVFLMVNGS	LLERLACA	HTPALTW		
Human IRAK4	286	HMRCKIAQGAANGINFLHENH	IHRDIKSANILLDEA	FTAKISDFGLARASEK	-FAQ	TVM	344	
Bovine IRAK4	NMRCKIAQGAANGLSYLHENH	IHRDIKSANILLDE	DFTAKISDFGLARASEK	-FAQ	TVM			
Mouse IRAK4	HTRCKVAQGTANGIRFLHENH	IHRDIKSANILLDK	DFTAKISDFGLARASAR	-LAQ	TVM			
Xenopus IRAK4	VLRCNIAYGTANGINYLHENS	HVRDIKSANILLDD	TLVPKISDFGLSRATGQ	-FSK	TMM			
Zebrafish IRAK4	RNRCWITVGAARGLSYLH	THAHIHRDVKSANILL	DGEFVAKISDFGLTRSAAAGSLMTLQ					
Human IRAK4	345	TSRIVGTTAYMAPEALRGE	ITPKSDIYSFGV	VLEIITGLPAVDEH	REPOLLLDIKEEIE	404		
Bovine IRAK4	TSRIVGTTAYMAPEALRGE	ITPKSDIYSFGV	VLEIITGLPAVDEH	REPOLLLDIKEEIE				
Mouse IRAK4	TSRIVGTTAYMAPEALRGE	ITPKSDIYSFGV	VLEIITGLAAVDEN	REPOLLLDIKEEIE				
Xenopus IRAK4	TERIVGTTAYMAPEALRGE	ITIKSDIFSFGV	VLEIISGLAPVDEN	RSPSLLLDIKEEIE				
Zebrafish IRAK4	TERIVGTTAYMAPEALRGE	ITAKSDVFSFGV	VLEIVLSGLPPVDES	SRDPA	LLLEMKDLD			
Human IRAK4	405	DEEKTIEDYIDKKMNDAD	STSV	EAMYSVASQCLHEK	KNKRPDIKKVQQLLEMTAS	----	460	
Bovine IRAK4	DEEKTIEDYVDRKMND	IDSTSIETMYSVASQCLHEK	KNKRPDIKKVQQLLEMTGS	----				
Mouse IRAK4	DEEKTIEDYTDEKMSDAD	PASVEAMYSAA	SQCLHEKKNRRPDI	AKVQQLLEMTAS	----			
Xenopus IRAK4	EEETIEEYTDKMGD	VEPNTLKKMYTVASQCLN	QMKNNRPVITRVLQ	NLEDIKNLVSSS				
Zebrafish IRAK4	DEDLSLLDF	TRRRQDWRTEELQIM	YEAASQCLCQKKNR	PAIAQVLSVLEDLHQKVISR				

Figure S4. Residues at IRAK4 Dimer Interface are Highly Conserved, Related to Figure 4

- (A) Surface electrostatics of α G and α H-I exo-sites at the IRAK4^{KD-D311N} dimer interface. The interfaces are composed of highly negatively charged α G helix and highly positively charged α H- α I loop. In the dimer, each surface is juxtaposed with the complimentary surface of its partner.
- (B) Alignment of IRAK4^{KD} orthologs from various species. Surfaces involved in IRAK4 dimerization, including the activation loop, α EF helix, α G helix, and α H- α I loop are highlighted in cyan, green, red and blue, respectively. Pink asterisks indicate sites of mutagenesis.

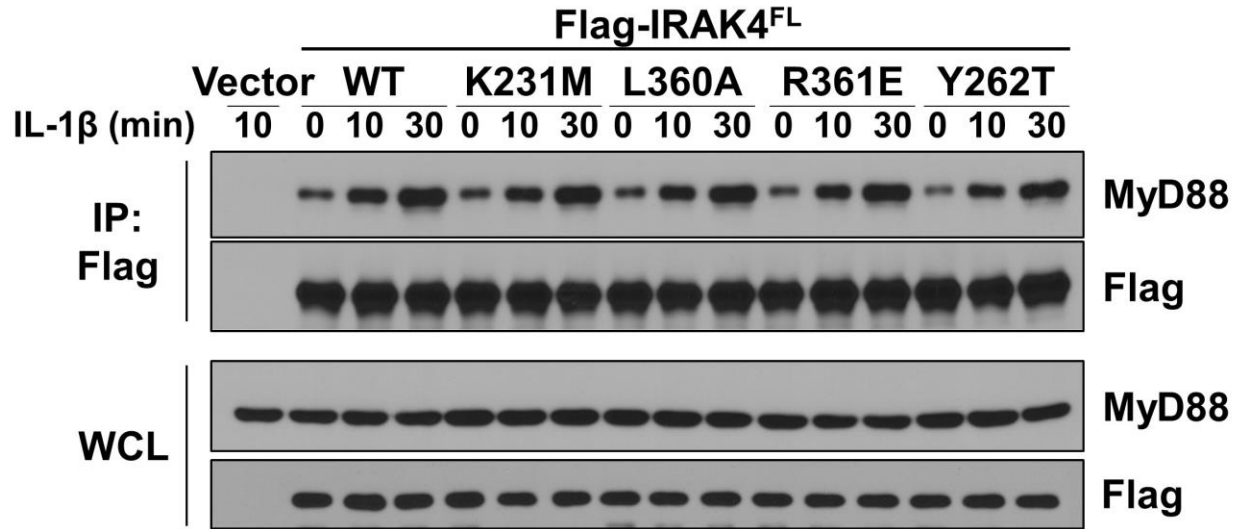


Figure S5. IRAK4 Kinase Domain Mutations do not Disrupt interaction with MyD88, Related to Figure 5

IRAK4-deficient human fibroblasts were infected with retroviruses containing empty vector construct (Vector), Flag-tagged IRAK4^{FL} wild-type (WT) and mutants (K213M, L360A, R361E, and Y262T). Cells were treated with IL-1 β (1 ng/mL) for the indicated times, followed by immunoprecipitation (IP) with Flag antibody and Western blot for MyD88. Western blot of whole cell lysate (WCL) was included to control for MyD88 and Flag-IRAK4 expression levels.

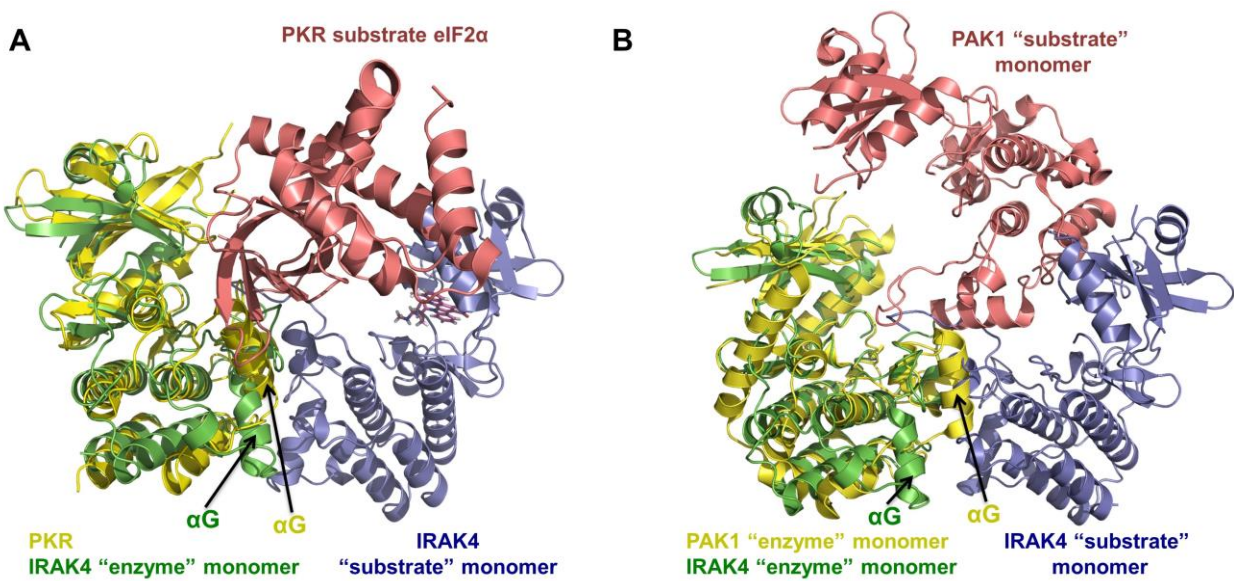


Figure S6. Comparison of the IRAK4 Asymmetric Enzyme-Substrate Dimer with PKR and PAK1, Related to Figure 7

- (A) The KD of PKR (yellow) is superimposed with the IRAK4^{KD-D311N} "enzyme" monomer. The PKR substrate eIF2α also interacts with the PKR αG helix. Similarly, the IRAK4 "substrate" monomer interacts with the IRAK4 "enzyme" monomer αG helix.
- (B) The "enzyme" monomers of PAK1 (yellow) and IRAK4^{KD-D311N} (green) are superimposed. The "substrate" monomers of PAK1 (pink) and IRAK4^{KD-D311N} (blue) are in distinct locations, illustrating the large differences between the dimerization interfaces.

SUPPLEMENTAL EXPERIMENTAL PROCEDURES

Cloning and Protein Purification

PCR fragments of human IRAK4, FL (1-460) and KD (154-460), were inserted into pFastBacHTB between BamHI and NotI restriction sites. Plasmids were transformed into DH10Bac™ *E. coli* competent cells followed by bacmid purification using the Bac-to-Bac® baculoviral expression system. Bacmids were transfected into Sf9 monolayer cells to generate baculoviruses. Harvested baculoviruses were used to infect High Five™ cells for 48 hours at 27 °C. Cells were harvested by centrifugation and resuspended in lysis buffer containing 50 mM HEPES-NaOH at pH 7.5, 300 mM NaCl, 10 mM imidazole and 1mM TCEP-HCl. DNase (10 µg/mL) and protease inhibitors (SIGMAFAST™ Protease Inhibitor Cocktail Tablets, EDTA-Free) were added to the lysate. Cells were lysed with an Avestin EmulsiFlex-C3 homogenizer. Cell debris was cleared via centrifugation at 48,400 relative centrifugal force (RCF). Clarified lysates were incubated with HisPur™ Cobalt Resin and washed extensively with lysis buffer. Bound proteins were eluted with lysis buffer supplemented with 150 mM imidazole. The eluates were immediately further purified with anion exchange chromatography using Source 15Q resin, followed by N-terminal 6xHis-tag cleavage using overnight incubation with 6xHis-TEV at 4 °C. When desired, IRAK4 was dephosphorylated via the simultaneous addition of 6xHis-λ-phosphatase and 5 mM MnCl₂. Removal of TEV and λ-phosphatase was facilitated with HisPur™ Cobalt Resin and anion exchange. IRAK4 was then further purified with a final size-exclusion chromatography (SEC) step in 20 mM HEPES-NaOH at pH 7.5, 150 mM NaCl and 1mM TCEP-HCl. Fractions containing IRAK4 were pooled, concentrated, and flash frozen in liquid N₂. To generate phosphorylated IRAK4^{FL} and IRAK4^{KD}, the proteins were incubated with 5 mM ATP and 10 mM MgCl₂ for 1 hour at 25 °C. Coexpression of His-IRAK4^{FL-D311N} and MyD88^{DD} (20-124) was achieved by insertion into pFastBacDual. Generation of bacmid, expression, and purification were performed as detailed above.

DNA containing MyD88 (20-154) and IRAK4 (4-106) was obtained by PCR and inserted into pET26 between NdeI and NotI restriction sites. The MyD88 G80K mutation and all IRAK4 mutations were introduced using the QuikChange II Site-Directed Mutagenesis Kit (Agilent Technologies). Plasmids were transformed into *E. coli* BL21-CodonPlus® (DE3)-RIPL competent cells. Cells were grown to an OD₆₀₀ of 0.6, followed by induction with 0.4 mM IPTG and overnight incubation at 20 °C. Cells were resuspended, lysed, and clarified as detailed above, without the addition of DNase or protease inhibitors. MyD88^{DD} (20-154), MyD88^{DD-G80K} (20-154), and IRAK4 (4-106) were then purified with HisPur™ Cobalt Resin followed by size-exclusion chromatography as detailed above.

Multi-Angle Light Scattering (MALS)

For molecular mass determination by MALS, protein samples were injected into a Superdex 200 (10/300 GL) gel filtration column (GE Healthcare) equilibrated with SEC buffer (above). The chromatography system was coupled to a three-angle light scattering detector (mini-DAWN TRISTAR) and a refractive index detector (Optilab DSP) (Wyatt Technology). Data were collected every 0.5 s with a flow rate of 0.5 mL/min. Data analysis was carried out using ASTRA V.

Sedimentation Equilibrium Analytical Ultracentrifugation (SE-AUC)

Experiments were performed in a Beckman Coulter Optima XL-A ultracentrifuge with an An-60 Ti rotor using six-channel centerpieces and quartz glass. Following SEC, IRAK4^{FL-D311N} was

diluted with SEC buffer to final concentrations of 6.4 μM , 4.8 μM , and 2.9 μM . Absorbance at 280 nm was collected, with SEC buffer serving as the blank. Samples were run at 4 °C. Sedimentation equilibrium was attained at speeds of 12,000 RPM, 15,000 RPM, 18,000 RPM, 22,000 RPM and 31,000 RPM. Data was processed with the programs Sedfit and Sedphat (Schuck, 2003) using a monomer-dimer self-association model. Buffer density and partial specific volume were calculated using the program Sednterp (Laue et al., 1992).

Crystallization, Data Collection and Structure Determination

IRAK4^{KD-D311N} at 10 mg/mL was incubated with staurosporine at a 2:1 molar ratio prior to setting up crystallization trays. Crystals were obtained by hanging drop vapor diffusion at 16-20 °C by mixing equal volumes of protein and reservoir solution (1.6-1.9 M ammonium sulfate, 100 mM Hepes-NaOH at pH7). Crystals were harvested, cryoprotected with reservoir solution supplemented with 20 % (v/v) ethylene glycol, and flash frozen in liquid nitrogen. Native data collection was performed at Brookhaven National Laboratory using the National Synchrotron Light Source (NSLS) beamline X29, while sulfur anomalous data was collected at NSLS beamline X4A. Data reduction was accomplished with XDS/XSCALE (Kabsch, 2010), followed by Ellipsoidal Truncation and Anisotropic Scaling (Strong et al., 2006) and solved by molecular replacement using Phenix (Adams et al., 2010). Model building and refinement were done with coot (Emsley and Cowtan, 2004) and Phenix (Adams et al., 2010). Figures were generated using Pymol (Delano, 2002). The final atomic model contains residues H166-L215, L226-S252, L258-A333 and T342-T458 in the “enzyme” monomer (A), and H166-A217, L226-D254, L258-F330 and V343-T458 in the “substrate” monomer (B).

Kinase Assays

Purified dephosphorylated IRAK4 was subjected to autophosphorylation and *trans*-phosphorylation experiments using [γ -³²P]ATP. IRAK4 samples at various concentrations were pre-incubated with or without 50 μM MyD88 G80K in kinase assay buffer containing 20 mM Hepes-NaOH pH 7.5, 150 mM NaCl, 1 mM TCEP, 10 mM MgCl₂, 50 mM Sodium Fluoride and 20 mM β -glycerophosphate for 30 minutes at 25 °C. Reactions were started by the addition of 5 mM [γ -³²P]ATP and incubated at 25 °C. At different time points, reactions were quenched by the addition of SDS-PAGE loading buffer containing 100 mM EDTA. Phosphoproteins were separated from free nucleotides on 12 % SDS-PAGE gels and visualized by autoradiography using a Fuji BAS-2500 apparatus. Incorporated phosphate was quantified by comparison to [γ -³²P]ATP dilution series using Image Gauge (FUJIFILM) software.

Biological Reagents and Cell Culture

Recombinant human IL-1 β was purchased from R&D system. Antibodies against I κ B α , MyD88, Mouse Anti-rabbit IgG (Conformation Specific) and phosphorylated I κ B α (Ser32/S36), JNK and IKK α / β (Ser176/180) were purchased from Cell signaling. Antibodies to Flag (anti-Flag) and to actin were purchased from Sigma and Santa Cruz Biotechnologies, respectively. HEK293/IL-1RI cells and human IRAK4-deficient fibroblasts were maintained in Dulbecco's modified Eagle's medium, supplemented with 10 % fetal bovine serum, penicillin G (100 $\mu\text{g}/\text{mL}$) and streptomycin (100 $\mu\text{g}/\text{mL}$).

Plasmids and Retroviruses

Human IRAK4 cDNA was purchased from Open Biosystems. The IRAK4 mutants were generated by site-directed mutagenesis polymerase chain reaction. The WT and mutants of IRAK4 were cloned into pMXs-IRES-Puro retroviral expression vector and transfected into

phoenix cells for viral packaging. Human IRAK4-deficient fibroblasts were infected by the packaged retrovirus for 3 days and selected by puromycin (2 µg/mL) for 2 days for stable viral integration. For all PCR reactions high fidelity Pfu Turbo polymerase was used (Stratagene).

Immunoblotting and Co-immunoprecipitation

Cells were harvested and lysed in a Triton-containing lysis buffer (0.5% Triton X-100, 20 mM HEPES (pH 7.4), 150 mM NaCl, 12.5 mM β-glycerophosphate, 1.5 mM MgCl₂, 10 mM NaF, 2 mM dithiothreitol, 1 mM sodium orthovanadate, 2mM EGTA, 1 mM phenylmethylsulfonyl fluoride and complete protease inhibitor cocktail from Roche). Cell lysates were then separated by 10% SDS-PAGE, transferred to Immobilon-P membranes (Millipore), and subjected to immunoblotting. For co-immunoprecipitations, cell lysates were incubated with 20 µL of protein A-Sepharose beads with anti-Flag antibody at 4 °C overnight, and beads were washed with 1 mL of lysis buffer 5 times before being dissolved in 40 µL of Laemmli buffer.

Quantitative Real-Time PCR

Total RNA was isolated using TRIzol reagent (Invitrogen). 3 µg of total RNA was then used for reverse transcription reaction using SuperScript-reverse transcriptase (Invitrogen). Quantitative PCR was performed in AB 7300 RealTime PCR System, and the gene expression of human IL-8, TNFα, and actin was examined by SYBR® GREEN PCR Master Mix (Applied Biosystems). PCR amplification was performed in triplicate, and water was used to replace cDNA in each run as a negative control. The reaction protocol included pre-incubation at 95°C to activate FastStart DNA polymerase for 10 min, amplification of 40 cycles that was set for 15 s at 95 °C, and annealing for 60 s at 60 °C. The results were normalized with the housekeeping gene β-actin. Primer sequences were designed using AlleleID 6.0. The following primers were used: human IL-8 forward, AGAGACAGCAGAGCACAC; human IL-8 reverse, GTTCTTTAGCACTCCTTGGC; human TNFα forward, TCAGCAAGGACAGCAGAG; human TNFα reverse, GTATGTGAGAGGAAGAGAACC; human actin forward, GTCGGTATGGGTCAGAAAG; human actin reverse, CTCGTTGTAGAAGGTGTGG.

Small- and Wide-Angle X-Ray Scattering (SAXS/WAXS)

To remove any aggregates and to ensure conformational homogeneity, the IRAK4^{FL}-D311N/MyD88^{DD} complex was purified with SEC immediately prior to SAXS. Data was collected at concentrations of 2, 1, and 0.5 mg/mL. Both small- and wide-angle X-ray scattering (SAXS/WAXS) data were collected in triplicate at NSLS X9 with an incident wavelength of 0.92 Å. SAXS and WAXS data merging, radial averaging, and buffer subtraction was performed with pyXS. Scaling and merging of data from different concentrations and Guinier analysis were performed with Primus (Konarev et al., 2003). Evaluation of the particle distance distribution function P(r) was accomplished with GNOM (Svergun, 1991) using a maximum linear dimension D_{max} of 212.5 Å. *Ab initio* modeling was performed with DAMMIF (Franke and Svergun, 2009). Twenty independent DAMMIF models were further processed with DAMAVER (Volkov and Svergun, 2003). The mean normalized spatial discrepancy (NSD) of the 20 independent models was 1.118 with a standard deviation (SD) of 0.110. One model was discarded due to an NSD greater than the mean + 2SD. The remaining 19 models were aligned, averaged, and filtered. Structures of the binary MyD88/IRAK4 DD complex (PDB: 3MOP) and IRAK4 KD dimers were placed into the resulting filtered volume. We then calculated the scattering profile of our fitted model using the program CRY SOL (Svergun et al., 1995) and fit it to the experimental scattering data.

Molecular Dynamics Simulations

Simulation systems were set up by placing the IRAK4 kinase dimer in a cubic simulation box (with periodic boundary conditions) of at least 97 Å per side and approximately 85,000 atoms in total. Explicitly represented water molecules were added to fill the system, and Na⁺ and Cl⁻ ions were added to maintain physiological salinity (150 mM) and to obtain a neutral total charge for the system. The systems were parameterized using the CHARMM36 force field with TIP3P water (Best et al., 2012; Jorgensen et al., 1983; MacKerell et al., 1998) and then equilibrated in the NPT ensemble at 1 bar and 310 K for 10 ns. Equilibrium molecular dynamics simulations were performed on the special-purpose molecular dynamics machine Anton in the NVT ensemble at 310 K using the Nose-Hoover thermostat (Hoover, 1985) with a relaxation time of 1.0 ps and a time step of 2.5 fs. All bond lengths to hydrogen atoms were constrained using a recently developed implementation (Lippert et al., 2007) of M-SHAKE (Kräutler et al., 2001). The Lennard-Jones and the Coulomb interactions in the simulations were calculated using a force-shifted cutoff of 12 Å (Beck et al., 2005).

SUPPLEMENTAL REFERENCES

- Adams, P.D., Afonine, P.V., Bunkoczi, G., Chen, V.B., Davis, I.W., Echols, N., Headd, J.J., Hung, L.W., Kapral, G.J., Grosse-Kunstleve, R.W., *et al.* (2010). PHENIX: a comprehensive Python-based system for macromolecular structure solution. *Acta Crystallogr D Biol Crystallogr* **66**, 213-221.
- Beck, D.A., Armen, R.S., and Daggett, V. (2005). Cutoff size need not strongly influence molecular dynamics results for solvated polypeptides. *Biochemistry* **44**, 609-616.
- Best, R.B., Zhu, X., Shim, J., Lopes, P.E., Mittal, J., Feig, M., and Mackerell, A.D., Jr. (2012). Optimization of the additive CHARMM all-atom protein force field targeting improved sampling of the backbone phi, psi and side-chain chi(1) and chi(2) dihedral angles. *Journal of chemical theory and computation* **8**, 3257-3273.
- Delano, W.L. (2002). The PyMol Molecular Graphics System.
- Emsley, P., and Cowtan, K. (2004). Coot: model-building tools for molecular graphics. *Acta Crystallogr D Biol Crystallogr* **60**, 2126-2132.
- Franke, D., and Svergun, D.I. (2009). DAMMIF, a program for rapid ab-initio shape determination in small-angle scattering. *Journal of Applied Crystallography* **42**, 342-346.
- Hoover, W.G. (1985). Canonical dynamics: Equilibrium phase-space distributions. *Physical Review A* **31**, 1695-1697.
- Jorgensen, W.L., Chandrasekhar, J., Madura, J.D., Impey, R.W., and Klein, M.L. (1983). Comparison of simple potential functions for simulating liquid water. *The Journal of chemical physics* **79**, 926-935.
- Kabsch, W. (2010). Xds. *Acta Crystallogr D Biol Crystallogr* **66**, 125-132.
- Konarev, P.V., Volkov, V.V., Sokolova, A.V., M.H.J., K., and Svergun, D.I. (2003). PRIMUS: a Windows PC-based system for small-angle scattering data analysis. *J. Appl. Cryst.* **36**, 1277-1282.
- Kräutler, V., van Gunsteren, W.F., and Hünenberger, P.H. (2001). A fast SHAKE algorithm to solve distance constraint equations for small molecules in molecular dynamics simulations. *Journal of Computational Chemistry* **22**, 501-508.
- Laue, T.M., Shah, B.D., Ridgeway, T.M., and Pelletier, S.L. (1992). Computer-aided interpretation of analytical sedimentation data for proteins. In *Analytical Ultracentrifugation in Biochemistry and Polymer Science*, S.E. Harding, A.J. Rowe, and J.C. Horton, eds. (Cambridge, UK: Royal Society of Chemistry), pp. 90–125.
- Lippert, R.A., Bowers, K.J., Dror, R.O., Eastwood, M.P., Gregersen, B.A., Klepeis, J.L., Kolossvary, I., and Shaw, D.E. (2007). A common, avoidable source of error in molecular dynamics integrators. *The Journal of chemical physics* **126**, -.

MackKerell, A.D., Bashford, D., Bellott, Dunbrack, R.L., Evanseck, J.D., Field, M.J., Fischer, S., Gao, J., Guo, H., Ha, S., *et al.* (1998). All-Atom Empirical Potential for Molecular Modeling and Dynamics Studies of Proteins†. *The Journal of Physical Chemistry B* 102, 3586-3616.

Schuck, P. (2003). On the analysis of protein self-association by sedimentation velocity analytical ultracentrifugation. *Analytical biochemistry* 320, 104-124.

Strong, M., Sawaya, M.R., Wang, S., Phillips, M., Cascio, D., and Eisenberg, D. (2006). Toward the structural genomics of complexes: crystal structure of a PE/PPE protein complex from *Mycobacterium tuberculosis*. *Proceedings of the National Academy of Sciences of the United States of America* 103, 8060-8065.

Svergun, D. (1991). Mathematical methods in small-angle scattering data analysis. *J Appl Cryst* 24, 485-492.

Svergun, D., Baraberto, C., and Koch, M.H. (1995). CRY SOL - a Program to evaluate X-ray Solution Scattering of Biological Macromolecules from Atomic Coordinates. *J. Appl. Cryst.* 28, 768-773.

Volkov, V.V., and Svergun, D.I. (2003). Uniqueness of ab initio shape determination in small-angle scattering. *Journal of Applied Crystallography* 36, 860-864.

IRAK4 Activation: A Cautious Embrace

Stevan R. Hubbard^{1,2,*}

¹Kimmel Center for Biology and Medicine at the Skirball Institute

²Department of Biochemistry and Molecular Pharmacology

New York University School of Medicine, New York, NY 10016, USA

*Correspondence: stevan.hubbard@med.nyu.edu

<http://dx.doi.org/10.1016/j.molcel.2014.09.003>

Structural and biochemical studies by Ferrao et al. (2014) in this issue demonstrate that dimerization of the kinase domain of IRAK4 is crucial for its activation, but with conditions: after—not before—receptor recruitment and before—not after—autophosphorylation.

Although eukaryotic protein kinases come in a limited number of catalytic (phosphoryl transfer) flavors—serine and threonine, tyrosine, or (most recently) histidine—they exhibit an impressive variety of regulatory mechanisms that transform a tepid enzyme (basal state) into an energized one (active state) and back again. The activation mechanisms include phosphorylation itself, either by the same kinase (autophosphorylation) or a heterologous one, and allosteric mechanisms (for an example, see Endres et al., 2011). Autophosphorylation can be either in *cis*, in which the kinase phosphorylates a residue in the same polypeptide chain, or in *trans*, one kinase phosphorylating a residue in a second copy of the molecule. Activation through *trans*-autophosphorylation is by far the more common mechanism, because in response to a biochemical signal, nature has found it more expedient to bring proteins together (facilitating a *trans* event) than to flip a switch within a protein (a *cis* event). In the study by Ferrao et al. (2014), the authors examined the activation mechanism for interleukin-1 receptor (IL-1R)-associated kinase-4 (IRAK4), a protein serine and threonine kinase that plays a critical role in signaling through Toll-like receptors (TLRs) and IL-1Rs (Kawai and Akira, 2010).

TLRs and IL-1Rs serve as sentries in inflammatory and innate-immune signaling pathways, recognizing pathogen-associated molecules such as double-stranded RNA, lipopolysaccharides, and unmethylated CpG DNA. A key feature of TLRs and IL-1Rs is that they oligomerize (see above regarding *trans* versus *cis*) upon engagement of their cognate ligands. IRAK4 is the first protein kinase to be recruited to the activated receptors, and

its recruitment is mediated by a so-called death domain (DD) in IRAK4 (N-terminal to the kinase domain), which binds to a DD in the MyD88 adaptor protein associated with the cytoplasmic regions of the receptors (Lin et al., 2010; Motshwene et al., 2009). Once recruited and activated, IRAK4 phosphorylates the downstream kinases IRAK1 and IRAK2, and the signaling pathway culminates in the activation of the NF- κ B pathway.

Like many protein kinases, IRAK4 is activated (i.e., its catalytic activity is stimulated) by autophosphorylation of the activation loop within the kinase domain, which causes a reconfiguration of the loop and the proper positioning of active-site residues. The IRAK4 activation loop contains three autophosphorylation sites, with Thr345 being the critical site for activation. Whether IRAK4 autophosphorylation occurs in *cis* or *trans* had been in question, and Ferrao et al. set out to understand the details of this initial autophosphorylation event. They expressed and purified a mutant version of the IRAK4 kinase domain for structural and biochemical studies, in which a key catalytic aspartate was substituted with asparagine, rendering IRAK4 catalytically dead. Surprisingly, they observed that the protein behaved as a dimer in solution, whereas the wild-type protein (which was phosphorylated as purified) was monomeric. Through a series of biochemical experiments, they determined that the kinase domain of IRAK4 (DD not involved) weakly dimerizes (dissociation constant of 2.5 μ M), but only when it is unphosphorylated.

These *in vitro* biochemical results set the stage for crystallization trials of IRAK4. Although crystallization of full-

length IRAK4 was the initial prize sought, because of persistent proteolysis between the DD and the kinase domain, Ferrao et al. settled for crystallization of the IRAK4 kinase domain (IRAK4-KD) in the unphosphorylated state (using the kinase-dead mutant). A crystal structure of phosphorylated IRAK4-KD was reported previously (Wang et al., 2006), which was monomeric (or at least no dimer of interest presented itself). Crystals of unphosphorylated IRAK4-KD were obtained, and of the various molecular interactions that constitute the crystal lattice, one dimeric arrangement of IRAK4-KD stood out: one in which Thr345 in the activation loop of one kinase domain was bound in the active site of another kinase domain. This immediately suggested that IRAK4 autophosphorylation occurs in *trans*, which they were able to confirm subsequently in a biochemical assay.

Another interesting feature of the IRAK4-KD dimer in the crystal structure is the nature of the interactions that mediate kinase dimerization distal to the active site (the so-called *exo* site). Residues in the C-terminal lobe of the kinase domain, in α helices EF and G, interact in a nearly symmetric (two-fold) fashion; that is, both the kinase domain acting as substrate and the one acting as enzyme contribute the same residues to the interface. Helix G is often involved in kinase-substrate interactions (Goldsmith et al., 2007), and in IRAK4, this helix is displaced significantly (independent of dimerization) from its usual position in a protein kinase (Wang et al., 2006). The IRAK4-KD dimer is reminiscent of the *trans*-autophosphorylating dimer captured in the crystal structure of p21-activated kinase-1 (PAK1) (Wang et al., 2011).

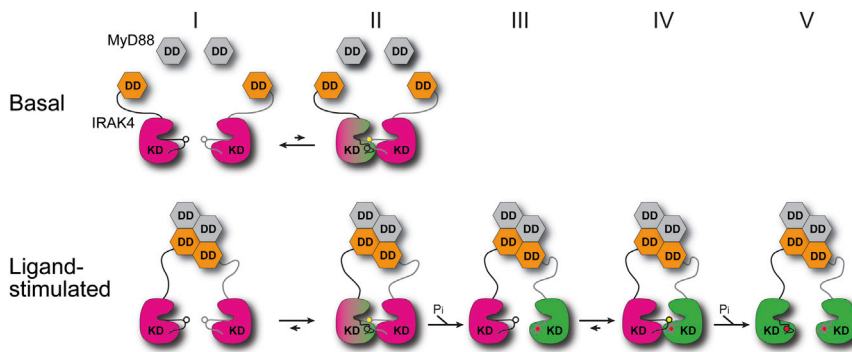


Figure 1. IRAK4 Activation through Kinase Dimerization

(Top) In the basal state, IRAK4 (death domain [DD], orange; kinase domain [KD], magenta, to depict low catalytic activity) is in the cytosol, predominantly as a monomer (equilibrium between states I [monomer] and II [dimer]). Thr345 in the kinase activation loop is unphosphorylated (open circle). (Bottom) Upon ligand stimulation and TLR or IL-1R oligomerization (not shown), MyD88 is recruited to the receptors, which in turn recruits IRAK4 via its DD. This favors dimerization of the IRAK4 kinase domains through a C-lobe interaction (state II). In this dimer, one kinase (magenta) serves as substrate, with Thr345 (yellow circle) bound in the active site of the other kinase (mixed magenta and green), which is transiently active (unphosphorylated activation loop adopts an active configuration). Phosphorylation (Pi, phosphate) of Thr345 (red circle) repositions the activation loop (state III), activating the kinase (green) and destabilizing kinase dimerization. The other IRAK4 kinase (magenta) can now be reciprocally phosphorylated by the activated kinase (state IV), and the two activated kinases, now monomeric, phosphorylate downstream substrates (state V).

Is the IRAK4-KD dimer observed in the crystal structure relevant *in vivo*? In a series of methodical biochemical and mutagenesis experiments, with corroboration from molecular dynamics simulations, Ferrao et al. showed that the interface visualized in the crystal structure indeed mediates IRAK4 dimerization and facilitates *trans*-autophosphorylation in solution. Furthermore, they showed that mutations in this interface mimicked the adverse effects of a kinase-dead IRAK4 in mediating downstream signaling events (NF- κ B pathway) in cells.

Other results presented in this thorough study will be of interest to protein kinase and IRAK4 aficionados, for example, the stabilizing role of the atypical gatekeeper

residue (tyrosine) in the back of the ATP binding pocket. They also performed small- and wide-angle X-ray scattering of the MyD88-IRAK4 core complex to generate a low-resolution structural model.

Putting it all together, Ferrao et al. provide the following scenario for IRAK4 activation (Figure 1). Prior to ligand engagement of TLRs or IL-1Rs, IRAK4 is in the cytosol in a monomeric state (owing to the weak kinase dimerization constant) and thus remains unphosphorylated with low basal kinase activity. Upon ligand-induced oligomerization of receptors, IRAK4 is recruited to the receptor-MyD88 complex via its DD. This translocation event greatly increases the local

concentration of IRAK4, which is sufficient to drive dimerization of the IRAK4 kinase domains. Reciprocal *trans*-autophosphorylation and activation of IRAK4 ensues, and the kinase dimer is destabilized, allowing substrates such as IRAK1 and -2 to gain access to the IRAK4 active site.

Thus, dimerization of the IRAK4 kinase domain is a critical “tipping point” in this cell-signaling system: too strong an interaction and IRAK4 would be activated prematurely and constitutively, and too weak an interaction would be insufficient to ensure *trans*-activation and signal propagation. Therefore, a cautious embrace is warranted.

REFERENCES

- Endres, N.F., Engel, K., Das, R., Kovacs, E., and Kuriyan, J. (2011). *Curr. Opin. Struct. Biol.* 21, 777–784.
- Ferrao, R., Zhou, H., Shan, Y., Li, Q., Shaw, D.E., Li, X., and Wu, H. (2014). *Mol. Cell* 55, this issue, 891–903.
- Goldsmith, E.J., Akella, R., Min, X., Zhou, T., and Humphreys, J.M. (2007). *Chem. Rev.* 107, 5065–5081.
- Kawai, T., and Akira, S. (2010). *Nat. Immunol.* 11, 373–384.
- Lin, S.C., Lo, Y.C., and Wu, H. (2010). *Nature* 465, 885–890.
- Motshwene, P.G., Moncrieffe, M.C., Grossmann, J.G., Kao, C., Ayaluru, M., Sandercock, A.M., Robinson, C.V., Latz, E., and Gay, N.J. (2009). *J. Biol. Chem.* 284, 25404–25411.
- Wang, Z., Liu, J., Sudom, A., Ayres, M., Li, S., Wesche, H., Powers, J.P., and Walker, N.P. (2006). *Structure* 14, 1835–1844.
- Wang, J., Wu, J.W., and Wang, Z.X. (2011). *Structure* 19, 1752–1761.